IEEE Access
Multidisciplinary | Rapid Review | Open Access Journal

Received June 2, 2016, accepted July 5, 2016, date of publication August 8, 2016, date of current version August 26, 2016.

Digital Object Identifier 10.1109/ACCESS.2016.2596761

Retinal Fundus Image Analysis for Diagnosis of Glaucoma: A Comprehensive Survey

M. CAROLINE VIOLA STELLA MARY[1], ELIJAH BLESSING RAJSINGH[2], (Member, IEEE), AND GANESH R. NAIK[3], (Senior Member, IEEE)

[1]Department of Information Technology, Francis Xavier Engineering College, Tirunelveli 627003, India
[2]School of Computer Science and Technology, Karunya University, Coimbatore 641114, India
[3]Faculty of Engineering and Information Technology, University of Technology Sydney, Sydney, NSW 2007, Australia

Corresponding author: M. C. V. Stella Mary (carolsam67@googlemail.com)

This work was supported by the University of Technology Sydney through the Chancellor's Post-Doctoral Research Fellowship under Grant CPDRF2013-16.

ABSTRACT The rapid development of digital imaging and computer vision has increased the potential of using the image processing technologies in ophthalmology. Image processing systems are used in standard clinical practices with the development of medical diagnostic systems. The retinal images provide vital information about the health of the sensory part of the visual system. Retinal diseases, such as glaucoma, diabetic retinopathy, age-related macular degeneration, Stargardt's disease, and retinopathy of prematurity, can lead to blindness manifest as artifacts in the retinal image. An automated system can be used for offering standardized large-scale screening at a lower cost, which may reduce human errors, provide services to remote areas, as well as free from observer bias and fatigue. Treatment for retinal diseases is available; the challenge lies in finding a cost-effective approach with high sensitivity and specificity that can be applied to large populations in a timely manner to identify those who are at risk at the early stages of the disease. The progress of the glaucoma disease is very often quiet in the early stages. The number of people affected has been increasing and patients are seldom aware of the disease, which can cause delay in the treatment. A review of how computer-aided approaches may be applied in the diagnosis and staging of glaucoma is discussed here. The current status of the computer technology is reviewed, covering localization and segmentation of the optic nerve head, pixel level glaucomatic changes, diagonosis using 3-D data sets, and artificial neural networks for detecting the progression of the glaucoma disease.

INDEX TERMS Glaucoma, age-related macular degeneration, Stargardt's disease, diabetic retinopathy, fundus image.

I. INTRODUCTION

MEDICAL image segmentation algorithms label each voxel in a digital diagnostic image to indicate the tissue type and provide information about the underlying anatomical structures. Inconsistent image quality, intensity inhomogeneity, blurred edges, and poorly defined boundaries are some of the inherent challenges encountered in the medical image segmentation task. Nevertheless, recent advances in the medical imaging modalities and computer vision contributed significantly to the growth of image guided diagnosis. In that vein, since the digital image data pertaining to the retina lends itself to the image processing and pattern recognition procedures, the early detection of retinal diseases becomes a reality. Before delving into the details of various retinal image analysis techniques, which is the main focus of this paper, what follows is a brief anatomical overview of the human eye with an emphasis to the retina. The most used among the five senses of the human body is the vision and the eye perceives most of the information about the world. A considerable portion of the brain is used in visual processing. The retina, a layered tissue lining the interior of the eye, converts the incoming light signal into a neural signal suitable for it to be processed by the brain. Rods and cones in the retina provide sensation of vision to the human eye, which includes color differentiation and perception of depth. Fig. 1 shows the anatomy of the eye. The retina consists of approximately one million nerve fibers, which group together to form the optic nerves. The beginning of the optic nerves in the retina is called the optic nerve head (ONH) or optic disc (OD), which is circular in shape and visibly bright in the fundus images. In one particular area there are no photoreceptors, namely, cones and rods, in the ONH, it cannot respond to

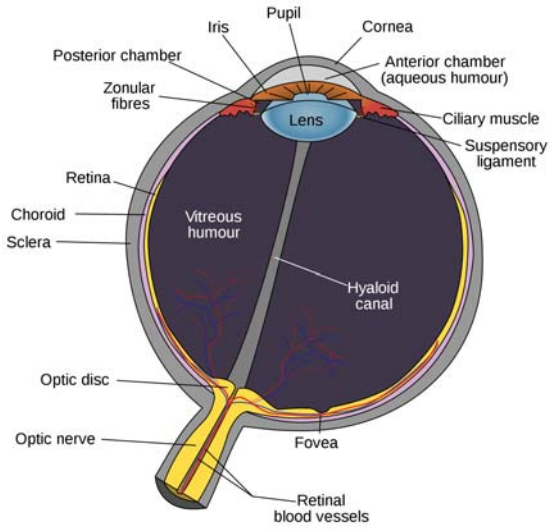

FIGURE 1. The anatomy of the eye showing the three main layers (retina, choroid and sclera), optic nerve, optic disc and varrious other features.

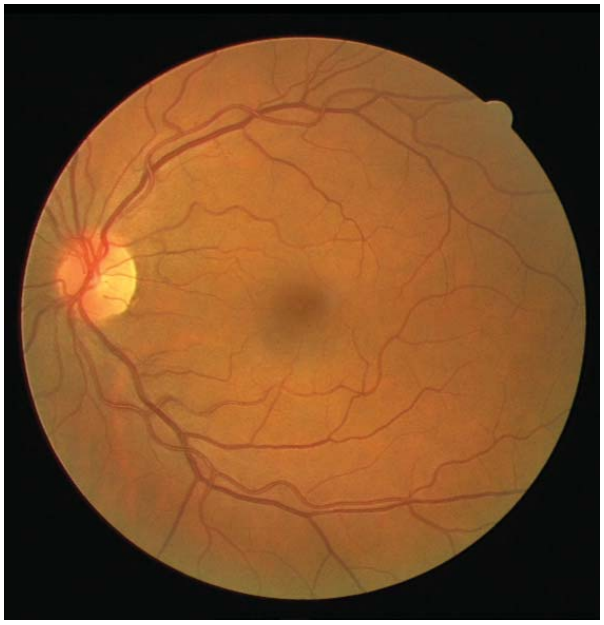

FIGURE 2. A Retinal Fundus Image [2].

the light stimulation, and hence known as the 'blind spot'. The optic nerves leaving the eye form a natural deep sloping region which is cup shaped, called the neuroretinal rim. The appearance of retina in normal fundus images is transparent and the retinal arterioles and venules run in the nerve fibre layer of the retina and are thus the only part of the retina readily visible on fundoscopy [1]. The reddish orange glow of the fundus is generated by reflection from the choroids, which is a rich network of blood vessels sandwiched between the retina and the sclera. Several diseases manifest themselves in the retina, a brief overview of the retinal diseases is presented below. Fig. 2 depicts an image captured through a fundus camera.

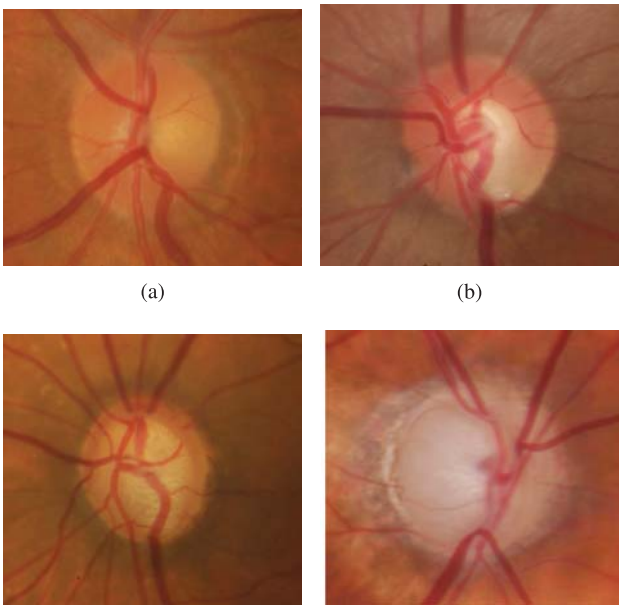

FIGURE 3. Retinal Fundus Images of the ONH - Normal and Pathological eyes [5]. (a) No Glaucoma. (b) Early Glaucoma. (c) Moderate Glaucoma. (d) Deep Glaucoma.

A. RETINOPATHY CONDITIONS

Glaucoma, a chronic disease that affects the optic nerves is the second major cause of blindness in the world leading to losses in the visual field and eventual blindness [3], [4]. Various risk factors associated with glaucoma have been identified, among which the significant one is the raised intra ocular pressure (IOP) that destroys the blood vessels and optic nerves. If glaucoma is left untreated, it may lead to permanent damage of the optic nerves and cause blindness. This progressive and irreversible damage to the optic nerves is often accompanied by only subtle signs or even no symptoms, and therefore it is nicknamed as the 'sneak thief of sight'. Fig. 3 depicts the different stages of glaucoma as it progresses. An early detection of glaucoma is important, which can minimize the damage and the vision loss, and ensure a prompt and adequate treatment. Changes in the structural appearance of the ONH and retinal nerve fiber layer (RNFL) often precede the development of visual field loss in glaucoma [6] in 3-D analysis. So far, such evaluation has predominantly been subjective and obtained with high intra and inter observer variability [7], [8]. With the emergence of newer optical imaging techniques, assessment of optic disc morphology has become more objective and quantitative. In recent studies, a large OD size [9] has been suggested as a risk factor for the retinal disease glaucoma. The ONH is a circular area where the optic nerve fibers converge, hence as the glaucoma progresses, it causes the nerve fibers to atrophy and results in apparent changes in the shape of the ONH. Often, variability in the appearance of the ONH caused by the image contrast and obscurity by blood vessels warrants a subjective manual screening and analysis. A quantitative relationship exists in between ganglion cell density [10] and visual sensitivity for

the detection of human clinical glaucoma. As an earlier means of diagnosis of glaucoma, investigators have suggested a variety of criteria [11] such as size of the cup, narrowness of the remaining disc rim, vertical ovalness of the cup, and progressive changes in the cup. If the position, center, and radius of the OD is detected precisely, it can in turn be used as a reference for locating other anatomical regions, for instance, macula and fovea. The patients who seldom complain of patchy loss of peripheral vision or reduced clarity of colours will in turn be followed up.

FIGURE 4. A Fundus Image with Diabetic Retinopathy [13].

Diabetic Retinopathy (DR) is a progressive pathology and is found in individuals who have diabetes mellitus for several years. It causes a group of lesions in the retina [12]. The number and types of lesions present on the retina determine the severity of the disease. It is a disease which is caused due to the insufficient insulin - a hormone that moves sugar from the blood into the cells. As a result, more sugar prevails in the blood which causes damage throughout the body including blood vessels. A fundus image with diabetic retinopathy is shown in Fig. 4. In DR, the blood vessels in the retina are affected and vision is lost. If left untreated, it can lead to blindness. An over accumulation of glucose and/or fructose damages the tiny blood vessels in the retina. The first lesions which occurs most frequently as a consequence of DR, is the Microaneurisms (MAs) that appears on the side of the blood vessels as small swellings [14]. During the initial stage, one does not notice any change in vision. A condition called macular edema is developed by some [15], which occurs when the damaged blood vessels leak fluid and lipids onto the macula which is the part of the retina that lets us see details. This fluid makes the macula swell and causes blurred vision. As the disease progresses, blood vessels start to proliferate. Lack of oxygen in the retina causes fragile, new blood vessels to grow along the retina and in the clear, gel-like vitreous humour that fills the inside of the eye. Without timely treatment, these new blood vessels can bleed, cloud vision, and destroy the retina. The longer a person has mellitus, the higher the risk of developing some ocular problem.

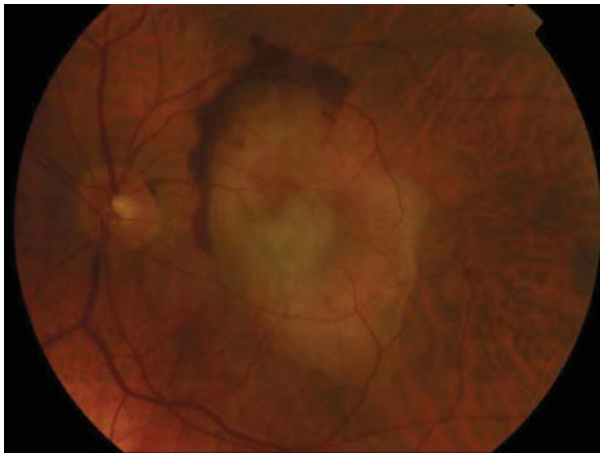

FIGURE 5. Fundus photograph showing an eye with neovascular Age-related Macular Degeneration [17].

Age-related Macular Degeneration (AMD) is a gradual, progressive, painless deterioration of the macula [16]. It is a leading cause of blindness and affects people, who are aged 65 and older. The appearance of spots beneath the retina marks the early stage of AMD. Fig. 5 shows a fundus photograph of an eye with neovascular AMD. These spots are small, round lesions called drusen that cause serious loss of vision. The loss of vision first starts in one eye, since the healthy eye will be compensating for the loss of vision in the damaged eye. It begins with characteristic yellow deposits (drusen) in the macula [18]. Most people with these early changes have good vision. People with drusen can go on to develop advanced AMD. The risk is higher when the drusen are large and numerous. Two forms of AMD exist: 'dry'and 'wet'. About 90 percent of those with AMD are affected by the former. Although irreversible, many patients with dry AMD experience no symptoms but experience only gradual and minimal changes in their vision clarity [19]. In wet macular degeneration, fine blood vessels at the back of the eye proliferate and leak fluid and blood. Wet macular degeneration may develop suddenly in patients with dry macular degeneration. Both forms of macular degeneration are painless and the condition typically affects both eyes. The Fig. 6 shows the range of vision under normal and pathological conditions for the same picture under different retinopathic conditions. But these vision patterns occur only at a latter stage, when these visions occur, and hence early diagonosis is very important in the case of ocular diseases. Hence, an automated diagonosis is essential for retinal diseases.

A new system, known as Retinal Image Vessel Extraction and Registration System (RIVERS), is used by retinal clinicians, researchers, and study directors as an integrated service for retinal image analysis over the internet [20]. We review the computer-aided techniques developed for the detection of glaucoma, a disease that occurs in the retina causing deformation of the ONH. An emphasis on how the ONH segmentation is carried out and the features and techniques used in determining the progression of glaucoma are discussed in this review.

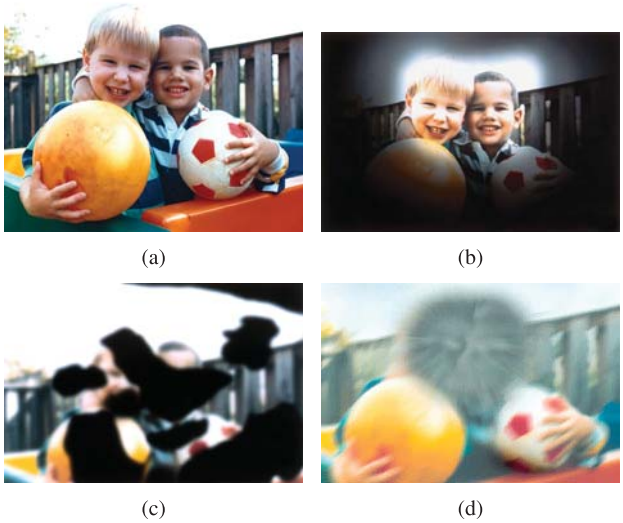

FIGURE 6. Signs and Symptoms of Glaucoma, DR and AMD. (a) A normal range of vision. (b) The same view with advanced vision loss from Glaucoma. (c) The same view with advanced vision loss from DR. (d) The same view with advanced vision loss from AMD.

II. IMAGE PREPROCESSING

Medical images usually contain noise due to interference and other phenomena, that affects the process of measuring parameters in images and data acquisition systems [21]. The minor differences that may be present in normal and abnormal tissues, due to noise and artifacts, make direct analysis in the images difficult. Shading artifacts due to nonuniform illumination degrades the efficiency of image analysis. Preprocessing is an essential step which reduces the image variation by normalizing the original image with a reference model. Preprocessing is required to eradicate noise present in the fundus image and equalization of the irregular illuminations associated with retinal images. It helps in reducing the intra image as well as inter image variability [22]. Pure glaucomatous changes are emphasized in the preprocessing step which excludes disease independent variations from the input images. These include variations due to image acquisition, such as inhomogeneous illumination or different ONH localizations and also retinal structures not directly related to glaucoma, e.g., the blood vessel tree.

A. ILLUMINATION CORRECTION

Nonuniform illumination is a general problem in retinal imaging due to the complexity of the optic system in the imaging process. Various techniques have been used in the removal of nonuniform illumination. Narasimha-Iyer *et al.* [23] used an iterative robust homomorphic surface fitting algorithm for the estimation of the illumination component and reflectance component in the removal of nonuniform illumination. Nyúl [24] compensated the illumination artifacts by a polynomial surface fitting technique by considering the intensity of the input image as a product of the luminosity and reflectance component. The low frequency changes of the image intensities here reflect the illumination inhomogeneities and this is applicable only for background regions and not for the retinal image features, as the least square polynomial fitting excludes these areas. But a percentile based thresholding identifies the structured regions as either brighter or darker regions. Yu *et al.* [25] viewed the image $f(x, y)$ as a product of an illumination component $i(x, y)$ and a reflectance component $r(x, y)$, which depends on the imaging surface. Equations 1, 2 and 3 denote how the new image is constructed from the image to be preprocessed.

$$f(x, y) = i(x, y) \times r(x, y) \tag{1}$$

The slow-varying background image is denoted as

$$f_b(x, y) = i_b(x, y) \times r_b(x, y) \tag{2}$$

and the resulting image is expressed as

$$\frac{f(x, y)}{f_b(x, y)} = \frac{(i(x, y) \times r(x, y))}{(i_b(x, y) \times r_b(x, y))} \tag{3}$$

It is assumed that the slow-varying background image is uniform over its surface, $r_b(x, y) = k$, and the illumination has been same for both the images. Then

$$\frac{f(x, y)}{f_b(x, y)} = \frac{r(x, y)}{k}. \tag{4}$$

The resultant image obtained is an illumination normalized image. Various adaptive techniques such as adaptive histogram equalization, adaptive Weiner filter and adaptive brightness schemes are used in the correction of the illumination. The adaptive histogram equalization [26]–[31] helps in enhancing the contrast of the image, while the adaptive Weiner filter [21] suggested by Bankman supresses unacceptable blurring of lines and edges. Wang *et al.* [32] stated that controlling the external lighting conditions [33] and adjusting the brightness of the images to a proper range has been difficult since there is a rise of intensity in some regions and reduced brightness as it lies far away from the OD. To enhance the darker regions, a brightness adaptive scheme is utilized, which is derived from the expression

$$y = \beta \times x^{\alpha} \tag{5}$$

where $0 \leq \alpha \leq 1$, x is the pixel value and $\beta = inmax^{\alpha}$, $inmax$ is the value of the upper limit intensity (i.e., brightness) of the input image ($0 \leq inmax \leq 255$). By the brightness adjustment function even dim areas can be identified. A proper selection of α and $inmax$ generates a curve as illustrated in Fig. 7. Balasubramanian *et al.* [34] utilized a normalization technique for correcting uneven illumination of a topography in Topography Change Analysis (TCA). Chrástek *et al.* [35] roughly estimated the illumination by median filtering using an optimal mask whose size is bigger than the retinal anatomical features, as larger masks tend to create problems at the image border. Youssif *et al.* [36] overcame the nonuniform illumination by an averaging function [27] where each pixel in the retinal image is adjusted using

$$I_{eq}(r, c) = I(r, c) + m + \bar{I}_w(r, c) \tag{6}$$

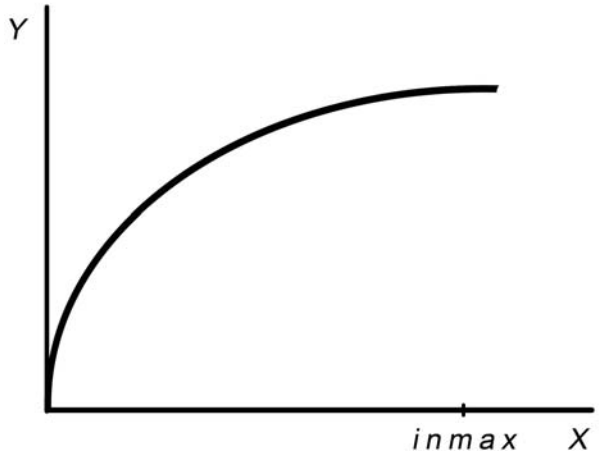

FIGURE 7. Expected function for brightness adjustment.

where m is the desired average intensity, $\bar{I}_w(r, c)$ is the mean intensity value in a window of size $N \times N$. The size of the window can vary from 30 to 50. Grau *et al.* [3] suggested a special inhomogeneity function for the compensation of illumination artifacts in the 3-D data sets. The OD region is found to be a bright yellowish than the other regions of the fundus image [37]. It shows better contrast in the red and green channels. The colour image is converted to a grayscale image using the following equation (7).

$$I_{RG}(x, y) = ((I_R(x, y))^2 + (I_G(x, y))^2)^{\frac{1}{2}} \tag{7}$$

The intra slice and inter slice variations in the 3-D data set is corrected using a third degree polynomial. Murray *et al.* [38] eliminated the preprocessing step by using the intensity as a function of instantaneous amplitude and frequency components, which helps in producing accurate results.

B. BLOOD VESSEL'S REMOVAL

Blood vessels act as distractors in the detection of OD and the removal of blood vessels is essential for proper detection of OD. Morphological processing is done as a preprocessing step prior to the detection of the location of the OD [30], [39]–[42] for the blood vessels and exudates present in the image to be filtered out. Hence the given RGB image is converted into a gray scale image since it shows good variation between the OD and the background. The blood vessels are darker and the OD is brighter. If exudates are present in the image, then this does not stand true. To remove the blood vessels and exudates from the retinal fundus images, morphological opening and closing is done using an appropriate structuring element. Opening suppresses bright details smaller than the structuring element and closing suppresses dark details smaller than the structuring element. Hence opening tends to smooth the contour in an image breaking narrow isthmuses and eliminating thin protrusion. Closing tends to narrow sections of the contour fusing narrow breaks and long thin gulfs and helps in generating vessel masks [24], which is followed by a morphological reconstruction. A shade correction operator is used to remove slow background variation, which is done by subtracting the background from the grayscale image. Osareh *et al.* [40], [42] used color mathematical morphology to extract important shape characteristics and relevant information. Low level features are extracted from the planes by Gaussians at different scales [43] and edge detectors. In colour morphological processing the L channel is taken from the *HLS* colour space where the blood vessels appear less strong than the normal intensity. When colour morphological operations are performed each pixel value is identified as a vector of colour components, with luminance L in the first position defined as: $x > y$ *if*

$$\left\{ \begin{array}{c} L_x > L_y \\ or\ L_x = L_y\ and\ S_x < S_y \\ or\ L_x = L_y\ and\ S_x = S_y\ and\ H_x \div H_o < H_y \div H_o \end{array} \right\} \tag{8}$$

The $\div$ operator gives a distance between two hue values on a unit circle and the hue values are measured based on a predefined origin. Morphological processing along with a shade correction operator helps in localizing the ONH appropriately and the results are promising and they perform better when compared to the existing techniques. Blood vessels originate from the OD and appear as deep red or orange red filaments that are of progressively diminishing width. The pixel values in the three color bands are strongly correlated [44], [45] and hence PCA is applied to diagnose the correlation coefficient matrix. The first axis correlates the main structural features, the second texture and the third, noise. The vessel/nonvessel separability is enhanced by using a canny edge detector as the first principal component, using the features like size, compactness and shape. Regions smaller than 30 pixels are reclassified as non-vessels. The ratio of square of the perimeter to area is used to segregate the non-vessels and if a region is found to be elliptic, the ratio of the major to minor axis is taken for the classification. Youssif *et al.* [46] used a simple edge fitting algorithm to segment the blood vessels and maximize the similarity between a predefined 2-D Gaussian template and the fundus image. Twelve 15×15 filters are generated along different orientations ($0°$ *to* $165°$) with an angular resolution of $15°$. To generate a binary vessel/nonvessel image, the maximum response from the global threshold selection algorithm proposed by Cao *et al.* [47], Otsu [48], and Yang *et al.* [49] is utilized.

Cheng and Huang [50] divided the original image into blocks, and for the estimation of a local threshold of each block, the corresponding gray-level histogram is utilized. As the global threshold approach generates too much noise, a local threshold is assigned depending on the gray-level value of the brightest 20% of the pixels. Noise reduction is done by using an edge detecting technique, where the adjacent pixels with gradients greater than ten are defined as edges. Using the threshold from the previous step, the points that are away from the edges are removed yielding the vasculature. Leel *et al.* [51] utilized a Gaussian kernel in the three

color bands for the smoothing of the image and to remove distractions.

C. BRIEF SUMMARY

Preprocessing is an essential process, as illumination artifacts are present in the retinal fundus images. Preprocessing methods improve the performance of image processing methods like segmentation, feature extraction, and pixel level glaucomatous changes. Manual control of illumination is inefficient and time consuming when capturing the images. Even the cameras have adequate artificial illumination necessary to preprocess the images before applying the image processing methods. Several preprocessing methods are available in the literature. Analysis of these reveal that illumination correction and removal of blood vessels, which act as distractors are to be carried out. Correction of illumination can be done by adaptive equalization and filtering techniques to enhance the contrast and to remove the blurring effects. Morphological processing can be done to remove blood vessels. To overcome some of the shortcomings, a vessel/nonvessel seperability procedure can be used for the removal of blood vessels. Hybrid preprocessing algorithms, with effective thresholding may yield promising results. If the resolution of the images is good, the preprocessing methods produce good results. An effective method has to be chosen, depending on the application and the preprocessing has to be done effectively even for the low resolution images. The preprocessing methods chosen may differ from application to application depending upon the requirements of the application process.

III. LOCALIZATION OF OPTIC NERVE HEAD

In retinal image analysis, accurately locating the OD is crucial to track the vessels and to register the changes in the OD due to the progression of a disease. The OD is a cluster of high intensity pixels and it is brighter than any other part of the fundus image. If exudates are present in the image in a darker background it also leads to be a candidate region of the OD.

A. HIGHEST IMAGE VARIATION

The intensity variations present in the image helps in locating the OD clearly. Hence, the contrast of the retinal image is enhanced by a locally adaptive transformation. The OD appears as a yellowish region [44] in the fundus image and it typically occupies approximately one seventh of the entire image. The appearance of the OD is identified by a relatively rapid variation in intensity as the 'dark'blood vessels are lying beside the 'bright'nerve fibres. The adjacent pixels variance of intensity is used in recognition of the OD. The retinal image is normalized and an average variance within the subimages of size $M \times M$ (usually 80×80 as the OD is of this size) are obtained and the location of the highest intensity of this image is taken as the centre of the OD, (i_d, j_d).

Eswaran *et al.* [33] utilized an averaging filter of size 25×35 pixels containing equal weights of one applied to the image region R_i in order to smoothen the low intensity variations, while leaving the objects of interest relatively unchanged whereas Chrastek *et al.* [52] used an averaging filter of 31×31 and the size of the ROI is taken as 130×130, where a canny edge detector is used in detecting the edges in the image. The green channel of the RGB color space is used in order to localize the OD. A contrast stretching transformation is used to make the bright object features more distinguishable from the background. This transformation slightly enhances the intensity values of the darker regions while the brighter regions of the image remain more or less unchanged. The average filter is applied to the gray scale image and the green channel of the fundus image. The contrast stretching is done in the green channel of the image. Fig. 8 depicts the above results. Abràmoff *et al.* [12] also suggested that the candidate regions for OD are selected by taking the highest 5% intensity level pixels and hue value in the yellow range. Then the nearby pixels are clustered to form the candidate regions. The clusters which are below a certain threshold value are abandoned. Liu *et al.* [53] divided the image into 64 regions and selected the region with the maximum of highest 5% pixels as the center of the ROI, as depicted in Fig. 9. The ROI is selected as the region with twice the typical OD diameter. Nyúl [24] suggested that an adaptive thresholding with a window size approximately the size of the vessel thickness is utilized. A mean filtering with the largest kernel and the threshold probing will roughly localize the ON. Chrástek *et al.* [35] stated that the ON can be detected using a proper threshold θ_{ONH}, calculated using

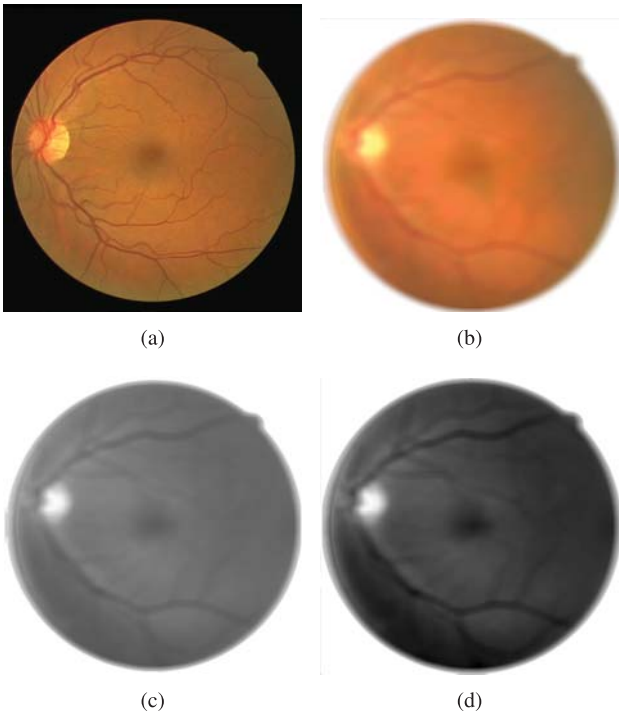

FIGURE 8. Averaged Contrast Stretching of Images. (a) Original Image. (b) Average Filtered Image. (c) Averaged Green Channel. (d) Contrast Stretched Image in Green Channel.

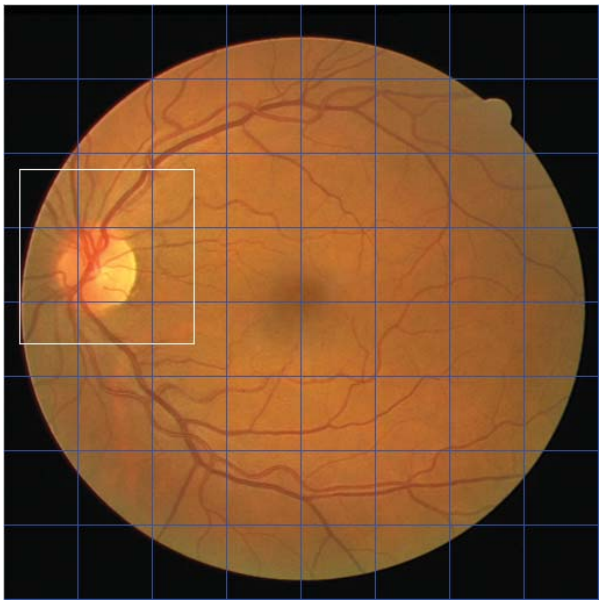

FIGURE 9. Image divided into 64 regions and ROI marked.

the mean gray value and standard deviation of all the pixels. The Euclidian Distance Map (EDM) removes noise and small regions. A threshold of 5 is used to remove the background, and the center of gravity of the remaining pixels gives the rough position of the OD. Li and Chutatape [54] used the highest 1% gray levels for clustering and the clusters with centroids within a specified distance are combined together. If the number of pixels in a cluster is less than 100, then the cluster is abandoned. The candidate regions are taken with 120 × 120 pixels and with the centroid as the center. Noronha *et al.* [55] used the highest 4% gray level pixels for the selection.

Leel *et al.* [51] used an unsupervised colour thresholding to initially classify the retinal image into a number of colour clusters. Unsupervised colour thresholding is a multithreshold segmentation procedure that applies a simple thresholding for each colour domain. It is generated by means of within class and between class criteria from the relevant colour band. After the unsupervised colour thresholding, clusters are weighted based on how similar the colour of the corresponding cluster is with reference to yellow. At times the cluster with the highest weight does not represent the OD object as in the case where the exudates appear as a brighter yellow than the OD. A second feature based on the level of the presence of blood vessels within a neighborhood is used, which is determined by a co-occurence matrix and weights are assigned to the second feature. Now the combinations of both the weights are determined and the one with the highest weight is classified as the OD. Fig. 10 shows how different candidate regions have been selected and the best candidate region is marked as the ROI. Cluster 1 has more yellow and a large amount of blood vessels are present. Hence Cluster 1 is classified as the ROI having the OD. The ROI is isolated from the background using a k-means clustering technique.

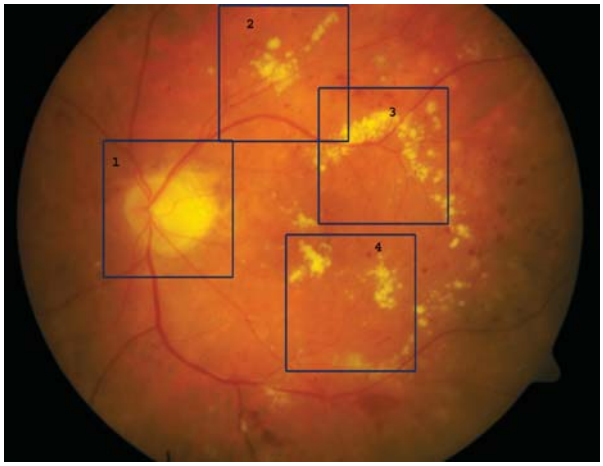

FIGURE 10. Candidate Regions selected by the color bands and the presence of blood vessels.

It uses the $L * a * b$ colour space [56]. The green channel of each fundus image is morphologically reconstructed using a circular structuring element [57]. Bright regions that are closer to the blood vessels are extracted as the candidate regions of the OD. The non-OD regions are classified using the 6 region-based features and a Gaussian Mixture Model classifier. A convex hull estimates all the candidate OD regions. The best-fit ellipse across the convex hull becomes the segmented OD boundary. The centroid of major blood vessels within the segmented OD boundary finally is detected as the Vessel Origin (VO) pixel location.

B. OPTIMUM THRESHOLD BASED LOCALIZATION

Siddalingaswamy and Prabhu [58] suggested that the OD is brighter than all other features in the retinal image, and it appears as a greater contrast in the green channel [33], [58]–[64] compared to the other two channels. Based on the approximation of the histogram of an image, an optimal thresholding method using a weighted sum of two or more probability densities with normal distribution is applied to segment the brightest regions in the image. The optimal threshold is obtained from the histogram of the image, which is scanned from the highest intensity value t_1 to a lower intensity value. The scanning stops at the intensity level t_2 which has at least a thousand pixels with the same intensity resulting in a subset of histogram. From this the optimal threshold is calculated as follows.

1) Initial estimate of T is calculated as

$$T_k = \frac{t_1 + t_2}{2} \tag{9}$$

2) Mean gray level of the object ${\mu_o}^k$ and background μ_b^k of the images are computed as follows

$$\mu_b^k = \frac{\sum_{i,j \epsilon background} I(i,j)}{no.\ of\ background\ pixels} \tag{10}$$

$$ {\mu_o}^k = \frac{\sum_{i,j \epsilon object} I(i,j)}{no.\ of\ object\ pixels} \tag{11}$$

3) New threshold is calculated as

$$T_{k+1} = \frac{\mu_b^k + \mu_o^k}{2} \tag{12}$$

4) Steps 2 to 3 are repeated until $T_k = T_{k+1}$

When this optimal threshold is applied to the image, it results in a number of connected regions. The region with the maximum number of pixels is taken as the OD region. Rosin *et al.* [65] performed dilation to remove the distractors and the image is divided into subregions and each region is weighted according to the summation of the variances. The various subregions are found in various locations, such as some lying completely on the background, some within which containing blood vessels and some without any blood vessels within them. Thus the candidate region is detected. Walter and Klein [66] applied a simple area threshold after morphological operations to obtain a binary image b that contains some parts of the OD as well as bright appearing pathologies like exudates. The biggest particle of the image b coincides with one part of the OD and its centroid c is calculated as the maximum of the discrete distance function of the biggest particle of b and is an approximation for the locus of the OD.

Cheng and Huang [50] utilized a adaptive thresholding technique to localize and segment the OD. The bright spot in the fundus image obtains the threshold T. The red channel is chosen, since it has minimal blood vessels as distractors in segmenting the OD. The object with the most 8-connected pixels is chosen. Since the variations in intensity is different for various images, an adaptive thresholding technique is chosen. The sliding band filter (SBF) is used [37] to downsample the image twice in order to reduce the computational cost. The first downsampling is applied to a larger ROI and the second to the smaller ROI. The highest filter response produces k-candidate points pointing to the OD candidate region. A local regression algorithm has been used for smoothing the boundary of OD. The OD center [67] is calculated using three distribution characteristics. They are local vessel density, compactness and uniformity.

C. MASK GENERATION

Mask generation [68] aims at labeling pixels belonging to the fundus ROI in the entire image. The dark surrounding region in the image are the pixels outside the ROI. Those pixels are not strictly dark (0 intensity value) but have to be discarded in subsequent processing stages. By calculating the statistics for each of the color bands of the image, a 4-sigma thresholding is performed with a free parameter empirically chosen such that pixels with an intensity value above that threshold are considered to belong to the ROI. A region connectivity test is performed for all the bands to be combined through logical operations and in order to identify the largest common connected mask. The ROI size is not always the same for each band. Fig. 11 shows a mask determined for Fig. 2.

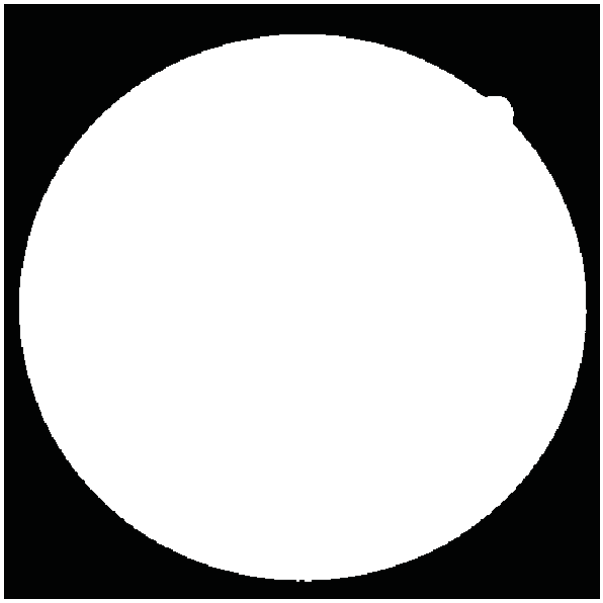

FIGURE 11. Mask determined for Fig. 2.

D. PRINCIPAL COMPONENT ANALYSIS (PCA)

Li and Chutatape [69] performed the PCA [24], [54], [70]–[72] on a set of training images containing the OD and extracted the dominant eigen vectors called 'disc space'- which represent the OD's significant features. To locate the OD in a given retinal image, the candidate regions are first selected by clustering the brightest pixels and applying the prior knowledge about the OD diameter. Then the distances between the candidate region pixels and their projection onto the 'disc space'are calculated, which are used to predict whether the pixels belong to the OD. Since large lesions areas usually distract in predicting the OD region incorrectly, the use of candidate regions aided in speeding up the processing, and the results are claimed to be robust even in the presence of large lesion areas. The size of the OD may vary and hence different scales are applied to find the pixel (L_x, L_y), as the OD center. The minimum distance in all the candidate regions and among all the scales is detected as the OD region.

E. HOUGH TRANSFORM

The OD is a bright and circular or elliptic region due to the photographic projection, morphological operations or edge detection techniques are attempted in a region of interest (ROI) enclosing the OD followed by the Hough transform for its localization [24], [30], [35], [39], [41], [46], [52], [66], [67], [71], [73]–[84]. A shade correction operator is used in the preprocessing step for the removal of slow background variations due to the exudates. The boundary and the center of the OD are estimated by applying the circular Hough transform, which maps any point (x, y) in the retinal image to a circle in a parameter space with center (a, b) and radius r that passes through (x, y) given by

$$(x - a)^2 + (y - b)^2 = r^2 \tag{13}$$

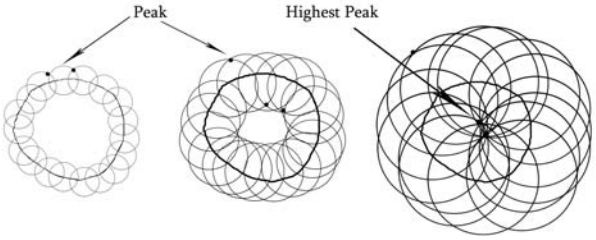

FIGURE 12. Hough Circles used in determining the Hough peak.

to all the feature points in the preprocessed edge map. In other words, by taking a feature point as the center, a fixed radius r in the feasible range can be used to construct a circle. Fig. 12 shows how Hough peaks are determined in the Hough circles drawn. Thus the set of all feature points give rise to circles, which may in turn intersect at an approximate center of a detected circular shape in the edge map for a suitable value of r, and as a consequence will produce a peak in the Hough space. Among the collection of circular shapes detected by the peaks in the Hough transform corresponding to various values of r, the *a priori* information about the OD's radius is made use of to select the most probable circle that closely resembles the boundary of the OD. Thus the method has proved to be very reliable in extracting the OD. Moreover, the selection of the correct candidate is preferred by the fact that the score of this algorithm is an absolute and not a relative measure.

F. LINE OPERATOR

The lightness component is used by Lu and Lim *et al.* [85] within the LAB color space [41], [86], [87], as the OD detection usually performs the best there. To enhance the circular brightness structure associated with the OD, the retinal image is smoothed using bilateral smoothing filter that combines geometric closeness and photometric similarity. A line operator is designed to detect the circular regions that have similar brightness structure as the OD. For each image pixel at (x, y), the line operator first determines n line segments L_i, $i = 1, \ldots, n$ of specific length p (i.e., number of pixels) at multiple specific orientations that center at (x, y) as shown in Fig. 13. Twenty different orientations are taken into consideration as illustrated in Fig. 14. For one specific orientation each line segment is divided into two line segments $L_{i,1}$ and $L_{i,2}$ both of the same length $(p-1)/2$ and hence the 'n' oriented line segments have 'n' image variations as follows. For $i = 1, \ldots, n$

$$D_i(x, y) = \left\| f_{mdn}(I_{L_{i,1}}(x, y)) - f_{mdn}(I_{L_{i,1}}(x, y)) \right\| \qquad (14)$$

Each line segment has a specific pattern which is used to locate the OD accurately. An orientation map $O(x, y)$ is constructed using line segment's image variation. This orientation map is converted to a peak image using

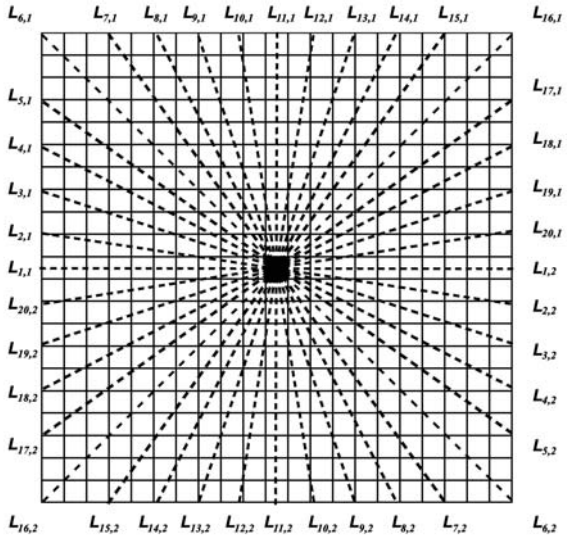

FIGURE 13. Example line operator that uses 20 oriented line segments.

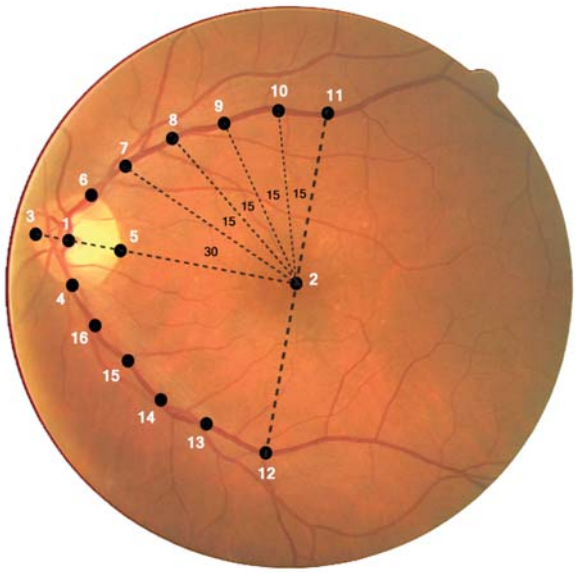

FIGURE 14. Model (PDM) overlaid on a retinal image.

a convolution map.

$$P(x, y) = \sum_{x=x_o-m}^{x=x_o+m} \sum_{y=y_o-m}^{y=y_o+m} M(x, y)O(x, y) \qquad (15)$$

Now the peak images are formed at the OD center and macula center and is classified into OD category or macula category depending on the image difference between the pixel at the center and those surrounding it. If the maximum score is obtained by the peak it is classified as OD and if it is a minimum, it is classified as macula. The score is determined by

$$S(x, y) = P(x, y)(Diff(x, y) \times (Diff(x, y) > 0)) \qquad (16)$$

where $(Diff(x, y) > 0)$ is the set of all image pixels with negative image difference to zero.

G. PYRAMIDAL DECOMPOSITION AND HAUSDORFF DISTANCE

1) PYRAMIDAL DECOMPOSITION

Lalonde *et al.* [59] used pyramidal decomposition [59]–[61], [68] to determine the potential regions which might contain the OD. He preferably used the green channel (G) in the original RGB image or the intensity channel in the HSI image, as they have the OD in a clearer form. For efficient implementation a Haar-based discrete wavelet transform is used in creating the pyramid. A four- and five-level decomposition of the image in the data set is performed and the resolution levels are adequate as only a few bright pixels fall into the original OD region. The pixels that have higher intensity values than the mean pixel value are considered to be candidate regions. Smoothing is done inside each of the candidate region and the brightest pixel is selected as a possible OD center point. CV_R, a simple confidence value, to assess the relevance of each hypothesis is defined as the ratio between the average pixel intensity inside a circular region centered on the brightest pixel of radius, which is approximately equal to the expected radius of the OD in the image and the average intensity in its neighborhood. It captures a circular patch of bright pixels surrounded by darker pixels. A rectangle slightly larger than the bounding box around the circular region is taken as the neighborhood. Potential OD regions, along with their confidence values CV_R and high-intensity pixel coordinates representing its center is obtained as the intermediate result for further analysis and the top ten candidates are retained. To locate the potential OD contours, an algorithm based on Hausdorff distance is utilized. The candidate regions identified by the pyramidal decomposition method are explored for the presence of a circular shape, as if the OD is a symbol in a map. Contiguous regions are aggregated into a single zone in order to limit the number of ROIs in the image.

2) OD CONTOURS USING HAUSDORFF DISTANCE

Binary images are given as inputs to the Hausdorff based matching technique. For each aggregated region obtained from pyramidal decomposition, perform edge detection followed by thresholding. Using the Rayleigh probabilistic modeling method detect the noisy edge distribution. After this a proper threshold has to be selected as it requires choosing a probability of misinterpreting a noisy edge as a true edge. The threshold T is estimated as follows:

$$T(x) = \left[(P_{FA}^{\frac{1}{M}} - 1) \sum_{j=1}^{M} x_j^2 \right]^{\frac{1}{2}} \tag{17}$$

where x_j's are the magnitudes of M noisy edge samples used for the estimation and P_{FA} is the probability of viewing a noisy edge as a valid edge. The estimation of T is done in the edge map using noisy edges only. The procedure adopted is as follows:

1) Canny edge detection [26], [47] is done using Canny hysteresis in the region of interest to capture as many edges as possible.
2) The high threshold is reassigned to a value that captures 10% of all edges in step 1 capturing the strong edges only.
3) The second edge map is subtracted from the first one to get the noisy edge map I_N.
4) M edge pixels are extracted within a small window in the center of the noisy edge map I_N to compute T for a given P_{FA}.
5) The final thresholded binary edge map I_T is obtained using the threshold T and is used for calculating the Hausdorff-based template matching.

The Hausdorff distance $H(A, B)$ is defined as

$$H(A, B) = \max(h(A, B), h(B, A)) \tag{18}$$

$$h(A, B) = \max_{a \in A} \min_{b \in B} \|a - b\| \tag{19}$$

where $h(A, B)$ provides a degree of mismatch between two sets of points A and B by measuring the distance of the point of A that is farthest from any point of B and vice versa. In a binary image I_T, A represents the set of black pixels and B the set of pixels that form a black circular template. The Hausdorff distance is calculated between the template and the underlying arrangement of pixels in I_T. If the match is exact, then the distance is zero which increases as the resemblance weakens. This even helps in locating the OD in the absence of precise disc borders and presence of vessels coming out of the disc. Two confidence values CV_H and CV_R are assigned to each Hausdorff candidate. CV_H, is the proportion of template pixels overlapping edge pixels in the thresholded edge map I_T. CV_R, is the ratio between the average pixel intensity over the template candidate and the average intensity over its neighborhood. This indicates how well the candidate is aligned with the OD from a pixel-intensity point of view and higher CV_R indicates better aligned candidates. For determining the best Candidate, the most likely OD position and radius are found by determining the candidate with the highest overall (global) confidence. The global confidence is chosen to follow the rule combination of the Dempster-Shafer theory, where the global confidence value CV_G is calculated as

$$CV_G = CV_H \times CV_R + CV_H \times (1 - CV_R) + CV_R \times (1 - CV_H) \tag{20}$$

H. A SPECIALIZED CORRELATION FILTER

Lowell *et al.* [88] integrated a specialized correlation filter [25], [89], [90] matching the OD structure for localization of the ONH. The correlation peak of the image gives the OD center. High intensity pixels are found near the circular rim of the OD with vertical oriented and a rough centrally located band of low intensity blood vessels. The template consists of a Laplacian of Gaussian with a vertical channel corresponding to the major vessel band in the middle. The intensity component of the fundus image is correlated with the template. A full Pearson-R correlation, which accounts for variations in mean intensity and contrast, is given by

the equation:

$$C_{i,j} = \frac{\sum_{x,y}(f(x,y) - \overline{f}(x,y))(w(x-i, y-j) - \overline{w})}{\sum_{x,y}(f(x,y) - \overline{f}(x,y))^2 \sum_{x,y}(w(x-i, y-j) - \overline{w})^2} \tag{21}$$

Several regions of interest have been identified by clustering algorithms because of several bright regions in the retinal images. A correlation filter is applied to each region for identifying the true region containing the OD. The final region of interest containing the OD is defined as an $n \times m$ rectangle whose center is the point with the higher response computed by means of the correlation filter. Due to the characteristic asymmetry of the ONH the filter is prone to locate a point slightly to the temporal side.

I. GEOMETRIC PARAMETRIC MODEL

The retinal fundus images have a common vascular pattern in almost all the images. The main vessels originate from the OD and they follow a specific course. They are geometrically modeled into two parabolas [67], [91], with a common vertex inside the OD. The vessels diverge when moving away from the OD, and branch vessels tend to deviate from the main vessel. The parabolas quickly bend towards the macula in the temporal region, whereas in the nasal region this inward deflection happens at a much slower rate. In order for the parabolas to be centered at the coordinates of the OD center (x_{OD},y_{OD}), a translation transformation had to be applied to the model.

$$x^* = x - x_{OD} \tag{22}$$

$$y^* = y - y_{OD} \tag{23}$$

Optimized values of parameters represent the best positioning of the OD, (x_{OD},y_{OD}) according to the model fit on the available data. The absolute minimum is found when (x_{OD},y_{OD}) are inside the OD, but in one of the many local minima the gradient-based algorithm would be easily trapped. To overcome this problem, a simulated annealing (SA) optimization algorithm has been implemented. SA is a global stochastic optimization algorithm that theoretically guarantees the convergence toward global minimum.

J. VESSELS DIRECTION MATCHED FILTER

Youssif *et al.* [46] used a threshold to the red band of the image [25], [71], [91], [92] along with the morphological operations. Each pixel of the green band is then equalized using the following equation.

$$I_{eq}(r,c) = I(r,c) + m - \overline{I}_w(r,c) \tag{24}$$

where m is the average density, $\overline{I}_w(r,c)$ is the mean intensity value of the pixels within a window size 40×40. The ROI of the retinal images is shrunk by five pixels to discard the pixels near the border since the amount of pixels used while calculating the local average intensity in the center is more than the amount of pixels used near the border. Adaptive histogram equalization is done to the illumination equalized inverted green band image. By recording the direction of the template that achieved the maximum response at each pixel, a vessels direction map (VDM) can be obtained from the segmentation algorithm. All the pixels labeled as nonvessel are assigned a '−1' in order to abstain from further processing. The binary vessel/nonvessel image is thinned to reduce the amount of pixels labeled as vessels into the vessels' centerline. All the remaining vessel-labeled pixels that are not within the square centered on each of the highest 4% intensity pixels are relabeled as nonvessel pixels. This step reduces the number of OD candidates. This detects the correct OD center in almost all the cases.

K. POINT DISTRIBUTION MODEL (PDM)

Given a set of parameters b, the PDM [69], [93], [94] can generate an s, and conversely also estimate b for a given s. As a result we have two spaces, an image space one in which s exists and a parameter space in which b lives. The PDM is linked to the image I by the cost function $F(s, I)$. The main axis of the model is defined by the points p_1 and p_2. Points on the vascular arch p_7 to p_{16} are positioned at fixed angles from the main axis. Two of the four points, p_3 and p_5, on the border of the OD lie on the main axis while the other two, p_4 and p_6, are located at the point where the venous vascular arch leaves the OD. By computing the mean model point position, the PDM is determined by

$$s = \frac{1}{n}\sum_{i=1}^{n} s_i \tag{25}$$

and the covariance matrix

$$s = \frac{1}{n-1}\sum_{i=1}^{n}(s_i - \overline{s})(s_i - \overline{s})^T \tag{26}$$

To find the s which best fits an image, the cost function must be minimized. The points can be moved directly in the image s or it can be done in the parameter space p of the PDM. In order to get the maximum optimization results, a combination of both the approaches have been taken into consideration. In the parameter space variations like rotation, translation, and scaling are done. In the image space the points are placed in the thickest most contrasted vessel. p_1 is found to be the center of OD and p_5 is found on the outer rim of the ONH. Fig. 14 depicts how the points are overlaid in the retinal fundus image. An automated method which is able to locate the most important anatomical landmarks in fundus images is presented here, which is able to find the OD and the macula in most of the cases.

L. VASCULAR DISTRIBUTION MODEL

To track the progress of the disease, it is imperious that the same retinal locations from one visit to another are measured [95]. Due to the movement of the patient, postural adjustments frequently occur during the OCT scan acquisition. When OCT magnifications are made even a small change may induce significant image displacements.

The Humphrey 2000 OCT system allows ocular motion to be viewed by means of a live monochrome video image of the ocular fundus as it is scanned. The video is obtained at the standard rate of 30 frames per second, interlaced scan. The appearance of the ONH which is a bright ellipse, elongated slightly in the vertical direction varies with the patients. Joshi *et al.* [80] utilized a pair of images, where the pair of images is divided into a reference image R and a floating image F. The circular Hough transform determines the region of interest from both R and F. The ROI is chosen as an 800×800 region centered on the OD from the green channel of both images, as it has better contrast than the other channels.

Retinal regions not containing the nerve head are called 'empty retina'. Eigen approaches can detect objects of a given class. Two classes of subimages C_N and C_R containing the eigen spaces ϕ_N and ϕ_R are selected corresponding to the subimages on the ONH and the 'empty retina'. Training images are taken to form the respective classes. A Hough transform has been used to identify likely image regions for the dual eigen space analysis by finding circles. The combined set of best circles for all radii is denoted (γ_i, c_i, ρ_i). Each region identified by the Hough circles is evaluated by extracting a 43×43 window, $\tau^*(\gamma_i, c_i, \rho_i)$ about its center (r_i, c_i) and projecting it on to the eigen vectors. Of the candidate locations at most five are forwarded for geometric analysis of their position with respect to the vessel contours. For each circle, these scores are then accumulated and weighted by π^i_{star}, a measure of the overall angular uniformity of the collective contour arrangement about (r_i, c_i).

$$v_i = \pi^i_{star} \sum_j v_{i,j} \tag{27}$$

The circle maximizing this measure is selected as the nerve head location. Any contour may contain points from a blood vessel, the nerve head perimeter, or both. While the vessels detected contain straight lines, the perimeter is curved. Using the mean-squared error it is first classified as either straight or curved in a straight line fit. The nerve head position is used to construct the vasculature distribution model. The responses accumulate coherently for those fields in which the nerve head detection is accurate.

M. EM FOR GAUSSIAN MIXTURE MODEL

Roychowdhury [57], Tan *et al.* [96], and Yousefi *et al.* [97] proposed a Gaussian Mixture Model (GMM), a probability distribution which assumes that the pixel intensities in the image can be modeled by a collection of K component Gaussian distributions with some mixing coefficient $\pi_k = 1, 2, \ldots, K$. The probability density function of each pixel, x can be represented as:

$$p(x) = \sum_{k=1}^{K} \pi_k N(x; \mu_k, \Sigma_k) \tag{28}$$

and the likelihood of the given Gaussian distribution is calculated using μ_k and π_k as the mean and variance of the k^{th} Gaussian distribution given by,

$$N(x; \mu_k, \Sigma_k) = \frac{1}{(2\pi)^{\frac{|x|}{2}} \sqrt{|\Sigma_k|}} \exp^{\left(-\frac{1}{2}(x-\mu_k)^T \Sigma_k^{-1}(x-\mu_k)\right)} \tag{29}$$

The mixture weight, π_k, must satisfy the following equation in order to have valid probabilities.

$$\sum_{k=1}^{K} \pi_k = 1 \quad and \quad \forall k : \pi_k \geq 0 \tag{30}$$

The data taken into consideration consists of $X=x_1,x_2,\check{E},x_n$ pixel instances occurring within the OD in the green channel. The green channel is selected as the visibility and contrast of the optic cup is superior in this channel. The pixel instances, x, are assumed to be independent, and stated as,

$$p(X|\pi_k, \mu_k, \Sigma_k) = \prod_{j=1}^{N} p(x_j) \tag{31}$$

In order to maximize the marginal likelihood in equation (31), we apply the expectation maximization (EM) algorithm for optimization in the GMM. For initialization of the EM-GMM parameters, neuroretinal rim, retinal vessels and optic cup are the features taken from the OD for processing. It is defined to have $K = 3$ Gaussians in the approach and equal weights for the mixture weight are initialized with $\pi_k^{initial} = \frac{1}{K}$. The EM algorithm estimates the number of Gaussian mixtures in its histograms and their corresponding parameterization. As each iteration progresses, the EM algorithm estimates the distribution of the hidden variable on each data sample (exp.ectation), and modifies the estimates of the Gaussian parameters maximizing (maximization) the joint distribution of the data and the hidden parameter. In the expectation step, the influence of each Gaussian responsible for x_j is calculated using the following equation

$$p_{jk} = \frac{\pi_k N(x_j; \mu_k, \Sigma_k)}{\sum_{i=1}^{K} \pi_i N(x_j; \mu_i, \Sigma_i)} \tag{32}$$

and in the maximization step the following parameters are re-estimated using the improved distribution of (32).

$$\mu_k^{new} = \frac{\sum_{j=1}^{N} p_{jk}\, x_j}{\sum_{j=1}^{N} p_{jk}} \tag{33}$$

$$\Sigma_k^{new} = \frac{\sum_{j=1}^{N} p_{jk}(x_j - \mu_k^{new})(x_j - \mu_k^{new})^T}{\sum_{j=1}^{N} p_{jk}} \tag{34}$$

$$\pi_k^{new} = \frac{1}{N} \sum_{j=1}^{N} p_{jk} \tag{35}$$

The EM process is re-iterated till the convergence of the likelihood function is satisfied.

N. BRIEF SUMMARY

Among the numerous methods available for localization of the ONH, though the Hough transform is a standard algorithm for line or circle detection, its computational complexity can be overcome by the fast Hough transform. One way of reducing the computation required to perform the Hough transform is to make use of gradient information that predicts in which direction a circle must lie from a given edge coordinate point. The optic disk is usually the brightest component on the retinal fundus images, and therefore a cluster of high intensity pixels will identify the optic nerve head location effectively. This works well, unless there are other potential fundus features such as exudates. The pyramidal decomposition method along with the Hausdorff distance compares the candidate regions to a circular template that approximates the optic disk, thereby selecting the appropriate candidate region. Vessel tracking techniques provide vital information about the center of the optic disk. The convergence of blood vessels also provides information regarding the center of OD. The diameter, position and direction of blood vessels helps the geometrical models to localize the center of OD. The first few principal components of PCA may also help in an accurate localization of ONH. For a proper convergence of the ROI, EM-GMM algorithm with new parameter values may be applied.

IV. SEGMENTATION OF OPTIC NERVE HEAD

After the accurate selection of the OD region, the active contours have to be drawn for the accurate detection of the OD boundary, as an accurate detection helps in assessing the progression of eye diseases.

A. ACTIVE CONTOUR MODEL

The usual segmentation algorithms are not enough to accurately find the boundary of the OD as they do not incorporate the edge smoothness and continuity properties. An active contour model [42], [83], [98]–[103], states that the presence of an edge depends not only on the gradient at a specific point but also on the spatial distribution. The curve adapts itself dynamically to the required edges or objects in the image. An initial contour is drawn to trace the OD using snakes. The snake moves under an evolution equation that pushes it towards configurations that minimise internal and external energies. The initial contour for a snake must be close to the desired boundary otherwise it can converge to the wrong resting place. Internal forces make the curve compact and external forces tend the curve towards the object's borders.

B. GEOMETRIC ACTIVE CONTOUR MODEL

Geometric computations are used implicitly in the geometric deformation model [58] for the evolvement of the curves. It starts with an initial curve that evolves its shape by minimizing the energy function represented by level set function π in the image domain. When the energy becomes minimum the curve evolution stops. In level set methods [53], [104]–[106], a contour is represented by zero level set function π and the energy function that is to be iteratively minimized to find the object boundary is given by an external energy function which has two values that fit the image intensities inside and outside the contour. The gradient descent method minimizes the energy function and it consists of a data fitting term, driving the active contour toward object boundary and the length term, producing a smoothing effect on the contour and the level set regularization term that controls the speed of the contour. Joshi *et al.* [80] used a region based active contour model [49] to improve the segmentation of the OD instances. This model uses the local image information at a support domain around each point of interest inspired by localized C-V models. The region-based method drives the contour using statistical information to decide whether or not a pixel should be aggregated into a region. The distractors such as blood vessels can influence the boundary-based deformable model's evolution. Tang *et al.* [107] utilized a C-V model to detect the contours both with and without gradient. This model uses a level set formulation and interior contours are automatically detected, and the initial curve can be placed anywhere in the image. In fundus images the papilla appears as a bright or yellowish region. Its shape appears more or less like a circle or an ellipse and it varies from image to image. Based on the shape feature, an elliptic shape restraint is imposed on the zero level set function of the C-V model.

Yu *et al.* [25] used a fast, hybrid level set model for a robust curve initialization as the Gradient Vector Flow (GVF) hybrid model. The curve evolution partial differential equation (PDE) is given by

$$\frac{\partial \psi}{\partial t} = g\epsilon k|\nabla\psi| + \beta_1(1-\lambda)|\nabla\psi| + \beta_2 \nabla g.\nabla\psi \qquad (36)$$

The first term is a front evolution driven by the internal curvature k. The second term represents a deformation driven by the region information I. For a bright target object, it indicates an expansion movement for the parts of the curve inside the object if $I > \lambda$ and a contraction movement for the parts of the curve outside the object if $I < \lambda$. The predefined threshold λ is the lower bound of the bright OD region intensity. The third term is the edge vector that helps to stop the evolving curve at the OD boundary. ϵ, β_1, β_2 are the parameters to control the balance of the forces.

C. GENETIC ACTIVE CONTOUR MODEL

Hussain [108] made use of the polar coordinates to simplify the implementation. A region of interest (ROI) is defined as the area bounded between R_{min} and R_{max} which is further segmented into four quadrants as designated by ophthalmologists - (I)nferior, (N)asal, (S)uperior and (T)emporal quadrants as in Fig. 15. A randomly chosen point in each quadrant is used as the initial population of snake points within this ROI in terms of radius $r(s)$ and an equally spaced angular displacement $\theta(s)$. Fig. 16 illustrates how as θ changes the

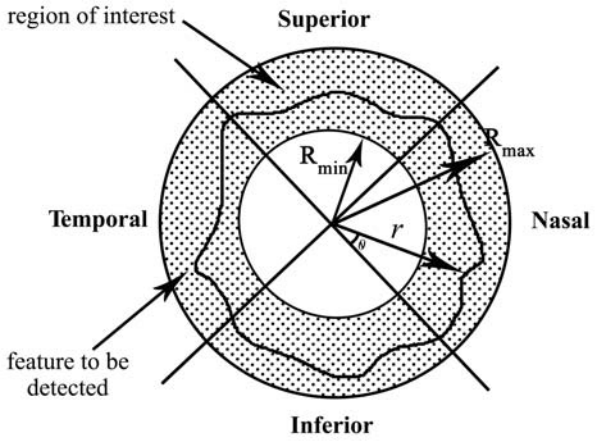

FIGURE 15. Snakes Space Parameterization.

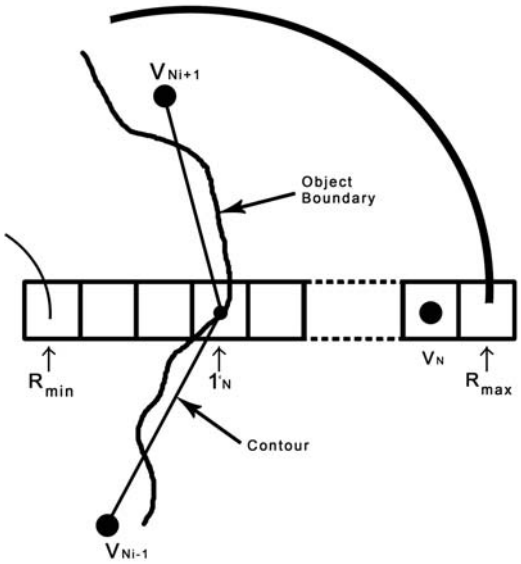

FIGURE 16. As θ changes the search space lies in all 4 quadrants.

search space lies in all 4 quadrants. Since the angles in the quadrant are multiples of one another, a change from 0 to $\pi/2$, may evolve the populations in the four quadrants in parallel.

D. GRADIENT VECTOR FLOW MODEL (GVF)

In the GVF model the snake equations for external energy are replaced by edge gradients [30], [42], [103], [109]. The external energy in the GVF model is by the equation (37)

$$V(x, y) = (u(x, y), v(x, y)) \tag{37}$$

The energy function to be minimized is given by

$$\gamma = \int \mu(u_x^2 + u_y^2 + v_x^2 + v_y^2) + |\nabla f|^2 |V - \nabla f|^2 dxdy \tag{38}$$

where f represents the edge gradients. The energy is mostly determined by the first term when $|\nabla|$ is small. In contrast, when $|\nabla f|$ is large, closer to the edges, the second term dominates and minimizes the energy making V almost equal to $|\nabla f|$. μ is a parameter that determines the relationship between smoothness of the vector field and how much the snake is attracted to the edges, and it represents the noise in the image. If μ is large, then a large noise is present in the image.

E. ACTIVE SHAPE MODEL (ASM)

Li and Chutatape [69] proposed the ASM, which utilized a PDM from the training set and an iterative search procedure to locate instances of shapes in the image under consideration. The shape instance is landmarked by the position of $n(n=48)$ where 14 points are selected on the main blood vessels $(1-8, 25-30)$ and the other points $(9-24$ *and* $31-48)$ are chosen evenly on the disc boundary. This ASM model is illustrated in Fig. 17. The shapes taken for training undergo transformations such as translation, rotation and scaling. The transformation parameters are obtained by minimizing the euclidian distance between the shapes using least square approach and then the aligned training shapes undergo PCA using the first four eigen vectors, which represent 93.22% of the total variance of the training shapes. One or two search zones may result from this aggregation for a retinal image of good quality.

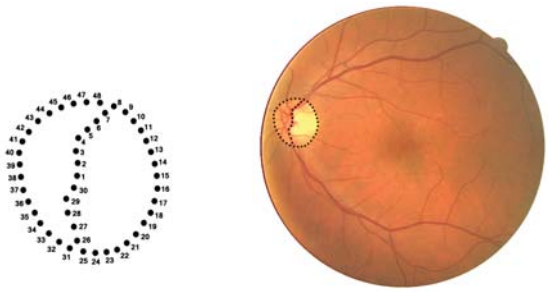

FIGURE 17. Active Shape Model. (a) A shape instance of optic disk. (b) Active Shape Model incorporated in the optic disk.

F. HU'S CIRCULAR MODEL

Hu's Circular model [88]–[90] is a combination of two models, the global model and the local model. The global model consists of a circle with center c and radius r. This is used for the rough fitting on the border of the disc. The local model is defined by a center c and evenly spaced radial spokes and direction vectors, $s_i = [cos(\theta_i), sin(\theta_i)]$. The model is defined by distances m_i from c along each spoke. The local model has a corresponding global model with radius $r = \overline{m}_i$ which is the local model's mean displacement. Three modification are made to Hu's model: A four phase algorithm has been designed for accurate segmentation. The first phase is the localization method. The Second Phase is the temporal lock. The third phase is the global fit. The fourth phase is the optimization for the improvement of the contour localization.

1) PHASE I - LOCALIZATION

A global elliptic model, that better fits to the elliptic shape of the OD with a vertical principal axis, and a fixed aspect ratio is used. The elliptical model can be transformed into an

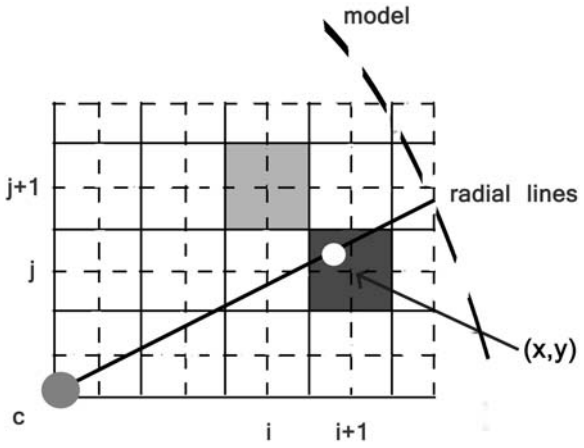

FIGURE 18. Bilinear interpolation of gradient.

equivalent circular model by scaling using the spoke ratios, to 'normalize'radial distances and forces. The vector gradient, is used to detect changes in the radial spokes intensity, and the radial gradient is calculated by the bilinear interpolation depicted in Fig. 18. The dot product of the gradient vector and the spoke direction vector determines the gradient with the spoke. The use of energy functions supports fast nonlinear optimization. The contour is altered under the influence of the force with external and internal components. External force drags towards the attractor points. The internal force is made up of the global and local force. The global force pulls towards the global shape whereas the local force smooths the model by penalizing differences in deformation between neighboring spokes.

2) PHASE II - TEMPORAL LOCK

A global model with 9 spokes is defined at angles $-60°$ to $+60°$ in steps of 15° on the temporal edge only. The gradient image is smoothed with a Gaussian filter. The temporal bias of the localization algorithm ensures that the initial contour is usually just outside the temporal edge. The radial search range is ± 6 pixels.

3) PHASE III - GLOBAL FIT

The whole phase is activated here using 24 spokes evenly spaced at 15°. The radial search range is ± 4 pixels. The other parameters remain the same as for phase II.

4) PHASE IV - LOCAL DEFORMATION

When the global model reaches equilibrium the local model is activated. To improve contour localization the gradient image is recalculated with smoothing factor. Local stage optimization is found to be more challenging than the global stage. This method detects the position of the major anatomical features of the retina [69], [93]. The algorithm output produces a vector, s_{result} which contains positions of 16 distinct points in the retinal image I. The parametric model is given by

$$s_{result} = G(b, F, I, O) \tag{39}$$

where s_{result} is the final output of the model, G, is the complete model b the set of parameters, F the cost function, I the fundus image and O the optimization algorithm. With the set of model parameters, b, the set of 16 points 's' has to be generated.

G. WARPING

Kim *et al.* [29] applied adaptive histogram equalization to the image and then used an average filter with 180 pixel-sized windows to smooth the sharpness of the image and detected the ONH center as the brightest point in the image. From the center of the OD an imaginary circle is drawn with the radius of one third of the distance between the center of the ONH and the fovea. The circle is then warped into a rectangle. At each 360° angles around the circle at 1° intervals from 0° through 359°, radial profiles are extracted. The rectangle-formed image consists of profiles of area in the circle centered at ONH. A thresholding technique performs binarization and every pixel having gray-levels less than half of the total level is discarded in the image. Pixels on each row having less than one third width of the image are removed and only the bottom pixels at each column are retained.

H. BRIEF SUMMARY

In this review geometric based active contours fused with level set methods tend to draw the active contours accurately. Improved performance can be found if Hu's circular model is utilized for the segmentation of the ONH. As stated by the various authors if preprocessing is done effectively, then distractors may not misguide the various contour models. The genetic active contours help in decreasing the processing time as the snake lithers through the four quadrants simultaneously. A combination of the active contour models can be tried with various level set methods to provide improvised results.

V. PIXEL LEVEL GALUCOMATOUS CHANGES

For detecting pixel-level glaucomatous changes [110]–[114] there are few methods:

1) Statistical Image Mapping (SIM)
2) Topographic Change Analysis (TCA)
3) Proper Orthogonal Decomposition (POD)
4) Vessel Diameter

A. STATISTICAL IMAGE MAPPING (SIM)

For glaucoma progression to be identified, the SIM method is employed wherein images are acquired at regular intervals of the clinical follow-up. A minimum of seven follow up examinations is required for the current SIM of the retina. The series of images are registered for a topographic height analysis at each individual pixel. The changes or stability of the pixels are summarized and a suitable statistic is derived from it. A line of best fit (slope) is derived from the ordinary least squares regression. The standard error of this slope indicates how well the data fits the linear trend. Now the test

statistic for each pixel is given by the absolute value of the slope divided by the standard error at that point. A large value of the test statistic indicates a large change in topographic height at that pixel. This process is repeated for all pixels and a statistic image is derived from it. The test statistic is recalculated by reshuffling the images randomly for all possible permutations of the order of the images. The glaucomatous structural changes affect a contiguous region in the ONH and the homogeneous regions are grouped together to form clusters. The permutation test is done pixel by pixel and the value is thresholded at 5% level with the pixels labeled as active or changing. After thresholding we are left with an image that will contain clusters of contiguous active pixels.

B. TOPOGRAPHIC CHANGE ANALYSIS (TCA)

For the assessment of glaucoma, in the TCA method, three Heidelberg Retina Tomography (HRT) images are acquired during each patient visit at regular intervals of the clinical follow-up. TCA compares the topographic height variability at superpixel (4 x 4 *pixels*) for a height change between the baseline examination and the follow up examination. For detecting a change in height variability in a superpixel, TCA utilizes topographic measurement from 16 different locations, and N different topograph scans acquired in each visit. An adjusted value is calculated by subtracting the respective topographic measurement in each pixel from its respective mean. The mean topographic height may be influenced by the location of each pixel in a scan and whether the scans are acquired at a baseline or follow up condition. The significance of change at each superpixel is evaluated using a Frequency distribution ($F-$distribution). The final step is to cluster contiguous and significant superpixel change locations for identifying progression from a baseline condition. The topographic changes compared are with the baseline and three consecutive sets of follow up images. Any patient, who showed a cluster of 20 or more significant superpixels bound within the contour line for the OD, is considered to have confirmed progression of glaucoma. A change in mean retinal height for each superpixel location gives the change in mean difference of the topography changes. The OD and optic cup are segmented using the superpixel [115] changes in the fundus image.

C. PROPER ORTHOGONAL DECOMPOSITION

The Proper Orthogonal Decomposition (POD) technique is used for detecting structural progression in an eye from a baseline condition. A bounded rectangular region covering a manually drawn OD is constructed in each of the topographies for selecting topographic measurements within the OD region. The changes are quantified using the parameters:

1) L_1 norm
2) Euclidean distance (L_2 norm),
3) Image Euclidean distance (IMED), and
4) Correlation

L_1 norm, L_2 norm and IMED parameters measure the degree of dissimilarity between a follow-up topography and its baseline subspace representation; lower values indicate more changes in the follow-up examination from the baseline. The glaucomatous changes in the OD region in the baseline and follow up visits are quantified using the above parameters. While using Euclidean distance for image similarity measurement performance degradation is primarily from the pixel-to-pixel correspondence used and this is due to the orthogonal coordinate system used for measuring an image distance. This drawback is overcome by the IMED, assigning a varying weight to the adjacent pixels using a non-orthogonal basis.

D. VESSEL DIAMETER

Vessel diameter also helps in identifying the progression of the disease. In order to detect the vessel diameter, first the vessel center line has to be detected. Vlachokosta *et al.* detected the vessel centerlines [116] by means of a differential calculus as the initial step. The vessels are found to be darker than the background. By finding the local minima of the image in the direction that is perpendicular to the vessel, the pixels that belong to centerlines can be detected. This can be seen from Fig. 19. The following properties hold for these pixels:

- The Hessian matrix (matrix of second order derivatives) of the image has at least one positive eigenvalue.
- The first derivative of the image across the direction of the eigenvector, which corresponds to the largest positive eigenvalue, vanishes.

The first acquired image is taken as the reference image and the other follow-up images are registered with respect to the reference one. For each image, the vessel centerlines are extracted and the distance transformation of the reference binary image is calculated,which provides the smallest distance of each pixel of the reference binary image from

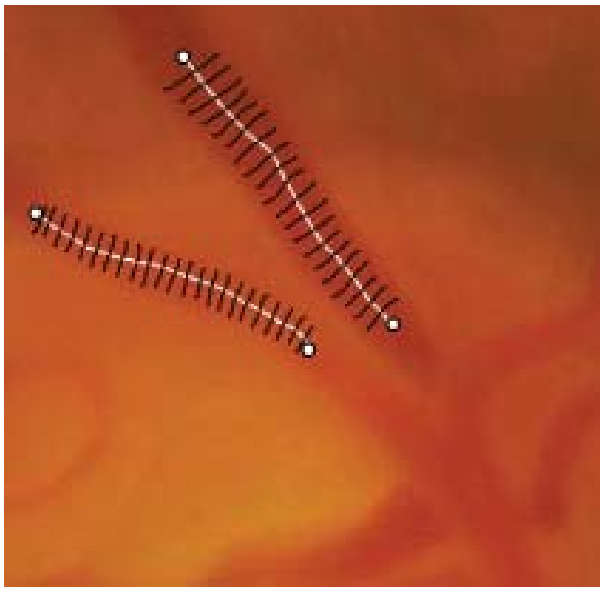

FIGURE 19. Vessel diameter estimation.

the centerlines. Then each image is transformed by an optimization process using the current values of the parameters of the transform. Estimation of vessel diameter is done by modeling the vessel intensity by means of Gaussian function. Due to the presence of a central light reflex in several vessels generated from a rough reflecting surface two models, with light reflex and without light reflex are described in order to best fit the observed vessels.

A robust M-estimation method determines the parameters of the model, since it reduces the effect of possible outliers on the estimation of the parameters. The vessel diameter is estimated by the difference of the abscissas that correspond to the zeros of the second order derivative of the model. However, the estimation of the diameter of a vessel that has light reflex is further complicated due to the fact that the roots of the second order derivative cannot be solved analytically. Therefore, the Newton-Raphson method is applied. For each selected vessel, the mean diameter and the standard deviation over the whole image sequence is computed and found that the vessel diameter is higher for images of patients who had ocular hypertension than the normal ones.

E. PROBABILITY MAPS

Soft classification method has been used by Narasimha-Iyer *et al.* [43] for the computation of the probability maps for a given set of features. A feature set F contains features $f_1, f_2, \ldots, f_n$. Each pixel (i, j) is represented by a feature vector containing the sampled features $f_1(i, j), \ldots, f_n(i, j)$.

To compute the k nearest neighbors for each pixels, the feature vectors can be input to a *kNN* classifier . The probability $P_c(i, j)$ for pixel (i, j) in class $c \in \{disc, bg\}$ is calculated as

$$P_c(i, j) = \frac{n_c}{k} \tag{40}$$

where n_c is the number of nearest neighbors of class c and k is the total number of nearest neighbors.

1) FEATURE SELECTION

A set of possible features has to be selected. This uses a one-time feature selection routine to optimize the feature set for the detection of the OD. A Sequential Floating Forward Selection (SFFS) algorithm serves this purpose and adds the best feature to the set. A Sequential Backward Selection (SBS) removes any feature that may degrade the performance, thus improving the overall performance of the selected set while reducing its cardinality.

2) POLAR TRANSFORMATION

The original transformation P_{disc} is transformed into polar coordinates. A kernel point Q is determined as the approximate center and this point should be available within the disc. The OD is sampled from Q radially outward with I rays of radius R and J samples per ray. The result of the transformation to polar coordinates is a new 2-D image $P(i, j)$ where $0 \leq i < I$ and $0 \leq j < J$. The samples are computed from an average of the values, excluding vessel pixels, along an arc whose endpoints bisect the surrounding two rays.

3) GRAPH CONSTRUCTION

The unwrapped image $P(i, j)$ can be viewed as a 2-D weighted, directed graph $G = (V, E)$ where each pixel corresponds to a vertex, V and edges E, the interconnection between these pixels. The boundary has to be smooth, and hence any two adjacent pixels on the border should not be too far apart. A smoothness constraint M exists in which a vertex V at the point (i, j) is said to have a directed edge from itself to every point $(i + 1, j \pm q)$ where $0 \leq q \leq \frac{M}{2}$ and $(j - q) \geq 0$ and $(j + q) < J$. The optimality of the path is defined with respect to the total cost of the vertices on it. The optimal path, computed in polar coordinates, consists of samples along the final border in the original image. The final border is calculated by transforming the samples using the inverse of the polar transform, and then fitting an interpolating 2-D closed spline to the data.

F. BRIEF SUMMARY

Pixel level glaucomatous changes may help in finding the progression of the disease. Instead of a single image, a series of images are used, and the changes with respect to the base line provide certain information about the disease progression. Proper orthogonal decomposition method using Haar based wavelet helps in providing information about the changes. The images have to go through transformation processes as the image will not be at the same position during each patients' visit. The super pixel level leads to more descriptive features and hence they are effective yielding significant computational savings. The pixel-wise change analysis technique of TCA analyze ONH topographies at $(1/4)^{th}$ of the original topographic resolution and requires two or more additional follow-up exams to confirm and establish confidence on a detected change. The POD framework uses only a single follow-up exam and analyzes the ONH structure at the original topographic resolution and detects glaucomatous changes from a baseline condition. Techniques such as TCA and SIM of the retina methods detect glaucomatous changes based on observed pixel changes within the optic disk margin.

VI. ALGORITHMS FOR 3-D DATASETS

Optical Coherence Tomography (OCT) [117]–[120] is a new imaging technique which produces micrometer-resolution, cross-sectional scans of biological tissues. Before the invention of Spectral Domain-Optical Coherence Tomography (SD-OCT), up to six B-scans or OCT slices are obtained from the optic nerve head during each scanning session. Then these slices are evaluated visually by the individual clinician. Some commercially available scanners acquires close-to-isotropic 3-D ONH-centered volumes. Isotropic [121] means that the size of each imaged element or voxel, is the same in all three dimensions. The cup-to-disc ratio and RNFL thickness is measured [122]–[125] here for accurate segmentation.

The 3-dimensional dataset produces the OD cube data composed of 200 A-scans derived from 200 B-scans. It covers a 6 × 6 mm area centered on the OD. The RNFL thickness map is created from the cube dataset. The software then automatically determines the center of the OD. It then extracts a circumpapillary circle (1.73 mm in radius) from the dataset to perform RNFL thickness measurements [126]. Mwanza *et al.* [127] utilized the Ganglion Cell Analysis (GCA) algorithm [127], [128] to discriminate the normal and the pathological eyes. It successfully detects and measures the thickness of the ganglion cell-inner plexiform layer. The fractal analysis (FA) [56] has been used in 1-D RNFL data. 2-D pseudo images are obtained from the 1-D RNFL data of both the normal and diseased eyes. The features are obtained from the FA, Wavelet Fourier Analysis (WFA) and the Fast Fourier Analysis (FFA). The FA features are found to be better classified than the other two. A random forest classifier classifies the cup, rim, and background using the three in-region cost functions [120]. Radial scans are created using the resampling of the volumes in which the Bruch's Membrane Opening (BMO) endpoints are easier to detect. The Haar Stationary Wavelet Transform (SWT) produces a radial projection image. The in-region and disc-boundary cost images are utilized by the multisurface graph-based approach to segment the boundaries of OD and cup. The multimodal approach outperforms the unimodal approach in segmenting the OD and the cup.

The introduction of the confocal scanning laser ophthalmoscope (CSLO), such as the Heidelberg Retina Tomograph (HRT), which obtains accurate three-dimensional images of the surface topography of the ONH helps in the early detection of glaucoma [129]. In order to examine for ONH changes, the confocal scanning laser ophthalmoscope (SLO) has become a useful tool in the morphological assessment of the ONH [130]. Area and volume derived topographic parameters have been used extensively for their ability to distinguish normal eyes from those with glaucoma. Paunescu *et al.* [131] used ONH parameters such as disc area, horizontal integrated rim volume, and vertical integrated rim area for the determination of whether glaucoma is present or not. During eye examinations, ophthalmologists [24] look for specific regions and patterns to identify possible markers of diseases.

The OD can be detected from a single OCT slice [132]. This method investigates the retinal pigment epithelium (RPE) which bounds the OD and which has a low-rank appearance structure that differs from areas within the disc. To segment the OD, it acquires from the OCT image an RPE appearance model that is specific to the individual and imaging conditions. This determines a low-rank dictionary from fundus image areas known to be part of the RPE according to prior knowledge of the ocular anatomy.

A. PREPROCESSING

Median filtering [133] is applied to the image which considers each pixel in the image in turn and refers to its nearby neighbors to decide whether or not it is representative of its surroundings. Instead of simply replacing the pixel value with the mean of neighboring pixel values, it replaces it with the median of those values. Rossant *et al.* [134] applied a non linear diffusion filter to the image, which performs better than median filters or Gaussian filters, since the edges are better preserved. The output image is then normalized between the values 0 and 1. The contrast between the inner retina and the vitreous is large enough to detect the Inner Limiting Membrane (ILM) by using an edge-tracking algorithm. This algorithm is based on the maximization of the local mean gradient. An active contour algorithm refines the result. The energy functions are defined by internal forces, the rigidity and the tension of the contour, external forces, and the GVF field derived from the gradient of the image. Abràmoff *et al.* [121] used a fast, three dimensional multiscale layer segmentation algorithm with a graph search approach. Surface 1 corresponds to the ILM, surface 2 lies between the inner and outer segments of the photoreceptors, and surface 3 is the outer boundary of the retinal pigment epithelium. When these three surfaces are segmented the approximate size, shape, and position of the ONH region is not yet known. A large region that is expected to include the ONH is excluded from surface detection.

B. EM ALGORITHM-ANISOTROPIC MARKOV RANDOM FIELD

Grau *et al.* [3] used three-dimensional datasets from monkey eyes under controlled intraocular pressure (IOP). He recommended that the hidden classification of images depends on a set of distributed unknown parameters. The E-M algorithm alternates between two tasks, classification of image voxels and estimation of distribution parameters, in an iterative way. The expectation and maximization are carried out at step $(t+1)$ applying the following equations:

E-Step:

$$p^{t+1}(x_i = k)|y_i, \theta^{(t)} = \frac{p(y_i|x_i = k, \theta_k^{(t)})p(x_i = k)}{\sum_j p(y_i|x_i = j, \theta_j^{(t)})p(x_i = j)} \quad (41)$$

where y_i is the log-transformed intensity at voxel i, x_i is the label given to this voxel, and $p(y_i|x_i = k, \theta_k^{(t)})$ correspond to a normal distribution

M-Step:

$$\mu_j^{(t+1)} = \frac{\sum_i y_i p^{t+1}(x_i = j|y_i, \theta^{(t)})}{\sum_i p^{t+1}(x_i = j|y_i, \theta^{(t)})} \quad (42)$$

$$\left\{\left(\sigma_j^{(t+1)}\right)^2 = \frac{\sum_i p^{t+1}(x_i = j|y_i, \theta^{(t)})(y_i - \mu_j^{(t)})^2}{\sum_i p(x_i = j|y_i, \theta^{(t)})}\right\} \quad (43)$$

In this way, the probability of the distribution, given the previous parameter values using Bayes' rule is estimated in the E-step and the new parameter values that maximize the probability is calculated in the M-step. The algorithm is guaranteed to increase the likelihood at each iteration thus converging at least to a local minimum. The use of

the structure tensor introduces local information about structure orientation and coherence into the segmentation process. An anisotropic Markov Random Field (MRF) [3], [31], [135] has been introduced in which the influence of neighbors on the classification of a voxel is weighted by the local structure characteristics at its location. The use of an MRF to determine the prior class probabilities increases the need for correct neighbor values. This method has showed improvement over the isotropic MRF.

C. RETINAL-VITREAL BOUNDARY

The retinal-vitreal boundary [136] helps in detecting the progression of glaucoma and is extracted first. Then this boundary is analyzed to determine the limits of the optic cup. The retinal-choroid boundaries are extracted to determine their endpoints, which lie on the optic disk perimeter. Significant contrast at the vitreal-retinal boundary is observed in the retina and optic nerve images. To make the retina homogeneous the speckle is suppressed and the contrast between the vitreous humor and retina is significantly increased. A brightness threshold t, that segments the retina and ONH from one side of the vitreous humor is found. Four basic operations are used by the boundary detection: noise reduction, columnwise edge detection, optimal threshold selection, and final boundary extraction. A 4×4 median filtering is used twice to preserve edges and edge locations. Speckle noise is often modeled as follows:

$$B(r, c) = I(r, c) \times N(r, c) \tag{44}$$

where $B(r, c)$ is a pixel in the B-scan, $I(r, c)$ is the actual pixel intensity, and $N(r, c)$ represents Gaussian distributed noise with a mean of one and a standard deviation σ_n. A Laplacian of Gaussian (LoG) edge detector is used and in one-dimension it reduces to the second derivative of the Gaussian. To compromise between the ability to localize weak edges and to suppress clutter, which impacts the detection error rate, a value of $\sigma = 5$ is chosen. The threshold value t which minimizes the cost function is determined using a sample $J(t)$ for a fixed set of t values evenly spaced over a range that always bounds t. The sampled minimum is found and a parabola is fit locally around this point

$$y(t) = at^2 + bt + c \tag{45}$$

The threshold t found in the image from the previous step, makes the matter of boundary extraction now insignificant. Noise in the vitreous humor can cause small artifacts to occur in the thresholded image. To remove these artifacts we first label each $4-$connected object in the image and remove those objects whose area is less than $\frac{1}{50}$ of the total area of all the objects in the image. The non cup regions are of constant curvature, but it is now assumed that the cup is parabolic rather than circular.

D. k-NN CLASSIFIER AND CONTEXTUAL k-NN CLASSIFIER

A fast multiscale extension of 3-D graph search is developed to detect four intraretinal surfaces in ONH-centered OCT volumes [43], [100], [137], [138]. The speckle noise is removed from the OCT volume by first ordering the voxel values according to their intensities. Then a combination of both the median filtering and averaging-based smoothing is done. Five gradient magnitude volumes are generated for different resolutions for the multi-scale approach, where level 4 represents the full resolution. For each level i, the $z-$values of the gradient magnitude volumes are controlled by the following equation:

$$z_{i-1} \times 2 - \alpha \leq z \leq z_{i-1} \times 2 + \alpha \; for 1 \leq i \leq 4 \tag{46}$$

where $z_{i-1} = f_{i-1}(x, y)$ is the surface segmented in level $i-1$ and α is a margin in z axis. The histological equivalent of the surface 1 is the Internal limiting membrane and the surface 2 is at the boundary between the inner and outer segments of the photoreceptors, and surface 4 corresponds to the outer boundary of the retinal pigment epithelium. Surfaces 2 and 3 are not present in the ONH region. The ONH has to be normalized across patients and in order to normalize it, the second intraretinal surface (surface 2) is used as it has a consistent shape over its surface. The second and fourth intraretinal surfaces are used to average the image in the $z-$direction for OCT projection of the image. The OD cup and rim are extracted from the background using a supervised classification method.

E. BRIEF SUMMARY

A logical extension of the work would be to derive 3-D medical image data for processing. The major disadvantages of the existing 2-D approaches can be solved by such an image driven approach, but the cost needed to develop automatic segmentation techniques is large, as the manual annotation process is too labour intensive and suffers from inter and intra observer variability. The 3D surfaces are reconstructed from 2-D contours detected in sequential 2-D images. The reasons behind the lack of interest on 3-D statistical surface models might be the low availability of adequate training samples, and the difficulties to design a proper modelling algorithm due to the complexity of 3-D shape variations.

VII. MACHINE LEARNING AND TRADITIONAL CLASSIFIERS

Glaucomatous variations among the images allows appearance based feature extraction. Transformation methods that provide information with different spatial and frequency resolutions are needed. Principal Component Analysis (PCA) reduces the high dimensionality of the transformed images into image-based features of lower dimensions. The goal of the machine learning [139] is to find an optimal classifier that has enough capacity to learn from the training data, and still be able to generalize the unseen data from the rest of the population in the input space. Let $x \epsilon R^d$ be an input feature vector, and let $y \epsilon \{-1, 1\}$ be its corresponding output label, for a two pattern classification problem [140], [141]. A machine learning classifier is modelled as a function $f(x, \pi)$ with a set of parameters π.

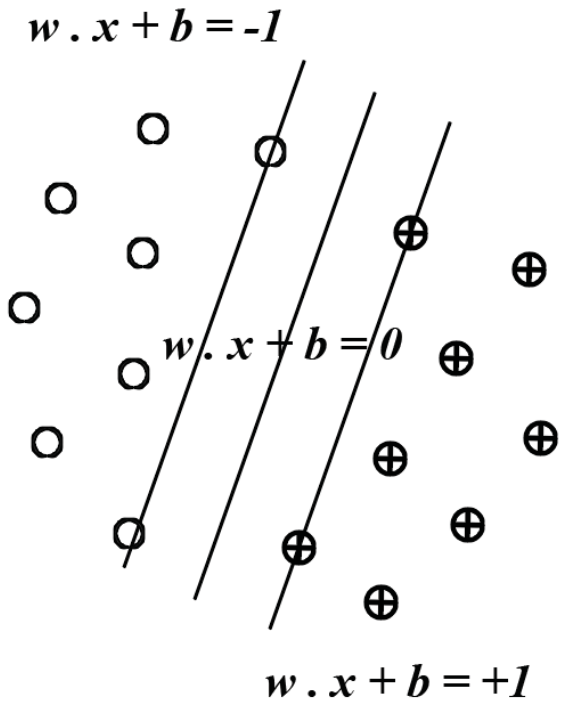

FIGURE 20. Support vectors in SVM.

A. SUPPORT VECTOR MACHINE(SVM

The SVM [139], [142]–[146] is a classifier which is generated with support vectors to form a classification decision hyperplane w with offset b which is based on the idea of structural risk minimization. The hyperplane is given by

$$hyperplane = \{|x|\langle w, x\rangle + b = 0\} \tag{47}$$

Input data x which fall on one side of the hyperplane are labelled as 1 and those on the other side as -1. Each classifier is generated from a different permutation of training and testing data from the same sample data. Fig. 20 shows how support vectors are determined in SVM. The structural capacity is estimated to be the same, since the permutation is statistically random and same sample data is used. Given a set of input feature $F = \{f_1, \ldots, f_d\}$, the feature vector is given by

$$x = \{f_1, f_2, \ldots, f_d\} \tag{48}$$

After this process, an optimal set of features $F_s = \{f_{s1}, \ldots, f_{sm}\}$ is selected representing a lower dimensional feature vector

$$x = \{f_{s1}, f_{s2}, \ldots, f_{sm}\} \tag{49}$$

where $m \ll d$ that can provide an optimal classifier. Once the optimal set of features are found, they are used to train the model for the final generation of the classification, whether normal or retinopathic condition.

B. DISCRIMINATIVE AND GENERATIVE CLASSIFICATION

In a two-class classification problem [142], a training set is given, consisting of $\{x_i, y_i\}$, $i = 1, \ldots, N$ where $x_i \epsilon R^D$ is the input, and it contains both continuous and discrete entries. The output label is determined by $y_i = \pm 1$. The Bayes' rule is the only consistent way to manipulate beliefs and plausibility and its classifier assumes independency between components of input. The classical linear discriminant analysis (LDA) [147] models the two classes of data with Gaussian densities of same variance but different means. It takes $D(D+1)/2 + D + D$ parameters in this approach. Linear discriminant function is determined by $u(x) = w.x + b$ which only needs $D + 1$ parameters results. If it is a dataset of finite size, fewer data points for each parameter is needed in the generative approach. Unless the equivariance assumption fits well to the data, the classical LDA will be less efficient, for the sole purpose of classification. The advantage of discriminative classifiers is that they concentrate mostly on the decision boundary, and they provide less insight into the structure of the data space and hence it is difficult to handle data containing missing entries. When performing the indirect classification [148] method there exists a relationship between the explanatory and intermediate variables, where $w = f(x)$ is unknown, therefore it has to be estimated. Based on the explanatory variables, models are created to predict the values of the intermediate variables. Then the classification is performed using the deterministically known classifying structure $g(w)$ between intermediate and response variables.

C. THE MULTI LAYER PERCEPTRON (MLP)

The MLP [142], [149], [150] is termed as a feedforward network, and is a generalization of single-layer perceptron. It is an approximation of any real valued function, and has three layers, the input, hidden and the output layers. In a two-classification problem the input x is given by $x = (x_1, \ldots, x_D)^T$, and

$$z_j = g\left(\sum_{d=1}^{D} w_{jd} x_d + w_{j0}\right) \tag{50}$$

$$f = h\left(\sum_{j=1}^{J} v_j z_j + v_0\right) \tag{51}$$

The activations of the hidden layer units are z_j, $j = 1, \ldots, J$ and w_{jd} are the weights between the input and the hidden layer. The weights connecting the hidden layer to the output unit are v_j. The terms w_{j0} and v_0 are the biases for the hidden and output units. The MLP is the most popular architectures among other neural networks, because it can be efficiently trained by error backpropagation. The mean-squared error (MSE) is not the proper error function in classification, but it is the negative log likelihood function. Despite having a different error function, the equations in the error backpropagation remain unchanged.

D. MIXTURE OF GAUSSIANS (MOGs)

Since the input of the glaucoma data contains only continuous values, each class-conditional density $p(x|C_\pm)$ is modelled by a normal multivariant density [142]. This results in a

classical LDA or a quadratic discriminant analysis (QDA), depending on whether or not the two normal densities are constrained to have the same covariance. Real data distributions usually do not follow a normal distribution but have slightly heavier tails, skewed or even a bi-modal structure. For such problems a single Gaussian is not flexible enough to model adequately the distribution of data. The MOG is very simple, and the probability densities for the positive and negative classes are each modeled first as a mixture of multivariant normal densities.

$$p(x) = \sum_{m}^{M} p(x|m)P(m) \tag{52}$$

$$p(x|m) = \frac{1}{\sqrt{(2\pi)^D|\Sigma_m|}} \times \exp\left[-\frac{1}{2}(x-\mu_m)^T \Sigma_m^{-1}(x-\mu_m)\right] \tag{53}$$

The expectation-maximization (EM) algorithm is used to find the parameters $P(m)$, μ_m and Σ_m. Multiple trials are required to avoid local minima. However, a learning rate is not required as the EM automatically chooses the optimal one.

E. MIXTURE OF GENERALIZED GAUSSIANS(MGGs)

The generalized Gaussian mixture model [142] models the class-conditional densities $p(x|C_{\pm})$ with higher flexibility, while preserving the possibility to realize the statistical properties of the data in terms of mean, variance, and kurtosis, etc., where kurtosis can be formally defined as the standardized fourth population moment about the mean. The MGG uses the same mixture model as the MOG, but each cluster is now described by a linear combination of non-Gaussian random variables s_m,which are the independent hidden sources in a cluster m responsible for generating the observation xs given A_m and b_m.

$$p(x|m) = \int \delta\Big[x - (A_m s_m + b_m)\Big] p(s_m) ds_m \tag{54}$$

s_m will assume a generalized Gaussian density of zero mean, unit variance, and shape parameter β_m,

$$p(s_m|\beta_m) = \prod_{d}^{D} \Big(s_{md}|\beta_{md}\Big) \tag{55}$$

$$p(s_{md}|\beta_{md}) = \omega(\beta_{md}) \exp\left[-c(\beta_{md})|s_{md}|^{\frac{2}{(1+\beta_{md})}}\right] \tag{56}$$

where $\omega(\beta)$ is the normalization constant and β is a measure of kurtosis. It will be adapted together with A_m, b_m and $P(m)$ during training.

F. PARZEN WINDOWS

The Parzen window [142] is a kernel-based nonparametric approach to density estimation given by

$$p(x) = \frac{1}{N}\sum_{i=1}^{N} \frac{1}{h_D} H\left(\frac{(x-x_i)}{h}\right) \tag{57}$$

where $H(u)$ is known as the Parzen window and has to satisfy $H(u) \geq 0$ and $\int H(u)du = 1$. If an isotropic Gaussian Parzen window is used as, $H(u) \propto \exp 1\frac{|u^2|}{2}$, it becomes a special instance of the MOG density estimation. Its dependency is mainly on the width parameter h. It provides only little information about the structure of the data and also requires storage of the entire training set for classification.

G. PIXEL INTENSITIES

Pixel intensity values are taken as high dimensional feature vector in standard appearance based approaches. Abràmoff *et al.* [138] utilized a Gaussian filter bank concept mathematically to create a larger set of features, from which an optimal combination of features could be selected. Gaussian filter bank features are sensitive to edges and textures in the gray-scale intensity image obtained from a color image at different scales and orientations. The outputs of a Gaussian steerable filter bank in hue, saturation, brightness space are taken as features and also the variance in the red, green, and blue channels in a small region around the pixel are taken as optimal parameters.

H. ONH SPATIAL FEATURES

A fundus camera is used to acquire a pair of sequential ONHPs in each subject [151]. Subjects' pupils are dilated, and photographs are taken at the leftmost and rightmost position of the pupil, to maximize the stereoscopic base. Tobin *et al.* [152] used a prior probability [153] with other statistical data for training of the localization of the ONH. A small set of fundus images that have had the ONH center manually selected is used for training. Using the prior probability the likely location of the ONH centre is determined for all patients for both the eyes. The retina is characterized in terms of the vessel structure as the vasculature emanates from the ONH. Four spatial features of the vasculature, the density map of the vessels $\omega(x, y)$, an average thickness map $t(x, y)$, an average orientation map $\theta(x, y)$ and a luminance map $l(x, y)$ are used to determine the center of the ONH. Mathematical morphology along with local linearity of vessels, piecewise connectivity and vessel brightness segments the vessels in the retina used. The vessel structures are dark relative to the retinal surface and hence the gray scale intensities are to be inverted. Two categories of rectangular convolution windows are chosen depending on the feature extraction. When the size of the convolution window matches the ON dimensions, the spatial feature characteristics are extracted using retinal luminance, vessel density, average vessel thickness and average vessel orientation as follows. Pederson and Anderson [154] used the cup-to-disc ratio [155] in determining the progression of the disease.

1) RETINAL LUMINANCE

This feature measures the brightness but it should not be confused with retinal lesions as they also appear as bright

objects thus determining the ON as it is a bright region

$$l(x, y) = I(x, y) \times w_1(x, y) \tag{58}$$

The size of the window is M x N = 1 ON diameter and it searches for brightness elements whose mean size is roughly equal to the ON diameter.

2) VESSEL DENSITY

The vessels enter the eye through the ON and they tend to be dense in this region. The density is defined as the no. of vessels in a unit area of the retina and the convolution window $w(x, y)$ is defined to be 0.6 ON diameter.

$$\rho(x, y) = b_t(x, y) \times w_v(x, y) \tag{59}$$

3) AVERAGE VESSEL THICKNESS

The vessels are found to be thickest near the ON. The thickness feature is independent of the no. of vessels in the window taken into consideration.

4) AVERAGE VESSEL ORIENTATION

The vascular orientation entering the eye is found to be roughly perpendicular to the horizontal raphe of the retina. They become more parallel as the distance to the ON increases. A steerable filter incorporating the second derivative of Gaussian and Hilbert's transform are used to determine the vessel orientation. To determine the conditional densities $p(v|\omega_{ON})$ and $p(v|\omega\neg_{ON})$, a vector $v[\rho, t, \theta, v]t$ is used. The prior probabilities $p(\omega_{ON})$ and $p(\omega\neg_{ON})$ are combined with the conditional densities $p(v|\omega_{ON})$ and $p(v|\omega\neg_{ON})$ for the calculation of posterior probabilities $p(\omega_{ON}|v)$ and $p(\omega_{ON}|v)$ using the Bayes' rule, which are used to develop a likelihood estimate for the location of the ON.

I. PARAMETER CLASSIFICATION

Swindale *et al.* [129] determined the shape of the ONH by a smooth two-dimensional surface with a shape described by ten free parameters such as cup position, cup radius, cup slope, cup depth, vertical offset, horizontal and vertical image curvature, nasotemporal slant and vertical slant. A least-square fitting method adjusted the parameters to give the best fit. The coordinates of a circular region that covered the cup are determined first. The following measurements are made:

- An overall measure of the steepness of the cup walls (g_r).
- Separate temporal (g_r^T) and nasal (g_r^N) components.
- A goodness-of-fit measure of the model to the image in this region (f_R): this value is larger in images in which the cup is irregular in shape.
- A goodness of fit measure of the image to a model without a cup (f_p): this value is larger in images with large cups and smaller in images with small or absent cups.
- A measure of maximum cup depth (z_{500}) is identified from the average of the 500 largest depth values present for image pixels within the cup region.

An analysis on the statistics of the different parameters enables to construct a classifier that gives the probability, $P(G)$, that each image came from the glaucoma population or not. Images are classified as abnormal if $P(G)$ >0.5.

Xu *et al.* [156] utilized a pair of stereo images taken from a conventional stereo camera. A four step analysis is carried out:

- 3-D ONH reconstruction [157], [158],
- disc margin detection,
- cup margin detection, and
- calculation of ONH stereometric parameters.

Depth is inversely proportional to the disparity between the two matching points from the left and right images in the stereo image pair. Disparity is defined as the coordinate difference (v_L-v_R) of the corresponding points. Multiple corresponding points are identified automatically on the left and right images by two matching methods namely the highest correlation, and the minimum difference of features. The various features include the gradient magnitude, gradient orientation, intensity, cross-correlation and feature difference between the given comparison windows, and detected the corresponding points at the location with the highest correlation and the minimum difference. Highest intensity on the image is located as the candidate region of the OD. The initial disc margin is detected with the Hough transform technique and refined by iteratively minimizing an energy function to converge properly. The combined information from the intensity value, image gradient, and boundary smoothness makes the energy function. The cup margin is located 150μm posterior to the disc margin for eyes with cup depths ranging between 0.2 and 1.0 mm. For eyes with cup depth shallower than 0.2 mm or deeper than 1.0 mm the cup margin is located at one fifth of the total depth. Seven ONH parameters such as disc area, rim area, rim volume, cup area, cup volume, cup-to-disc (C/D) area ratio, and vertical C/D ratio-were automatically generated.

J. FEATURE SELECTION

1) MOMENT METHODS

Confocal Scanning Laser Tomography (CSLT) captures 3-dimensional ON images for the automatic analysis, to provide support in the clinical care of patients affected with glaucoma. The back of the eye is scanned sequentially in two dimensions, and a series of images is captured. In each of the image series, the relative height of the retinal surface structure is inferred by finding the focal plane in which maximum reflectance of each pixel occurs (topography image). Moment Methods [159], [160] are used to extract features from CSLT images. Moment features are properties of connected regions in binary images that are invariant to image transformations and with respect to its axes, describes the image content and captures both global and detailed geometric information about the image. Zernike moments are utilized where the image's properties are described by their order (n) and repetition (m) with respect to a digital image. The low order

moments capture gross shape information and high order moments incrementally resolve detailed information of the digital image. If more information is present in the image, then it may add to some noise. So higher order moments usually do not contribute much information and the task is to determine the optimal number of lower order moments. For the Zernike moments generated, the order n and repetition m meet the conditions, $n - |m| = even\ and\ |m| \leq |n|$. Now a proper selection of optimal subset features is essential, hence Multilayer Perceptron(MLP) and Support Vector machines (SVM) based wrapper models are used to find an Optimal Moment Feature Subset (OMFS) to provide optimal data classification accuracy. In order to determine the size of the OMFS, an accumulative feature selection strategy is used which incrementally adds moments to an existing feature set and train a classifier (MLP and SVM) to determine the classification accuracy for the new feature subset. All the moments are normalized in the range $[-1, +1]$.

2) EUCLIDEAN BASED FEATURE SELECTION (EUBAFES)

Feature selection based on a distance based feature [161], is constrained to reinforce similarity between instances that fall into the same class, and decay in similarities between instances that fall into different classes. To solve the problem, an energy function which determines which feature subset is superior to the other has to be found. We need an optimal search algorithm to avoid exhaustive search, because the number of possible feature subsets grows exponentially with the number of features. The search space is defined by a hypercube, where the optimal search continues by hopping through the corners with a specific strategy. The energy function used here depends on the inter and intra class similarities. This method does not select all features with discriminant properties but selects a subset of features that together have a best discriminant property.

K. BRIEF SUMMARY

Artificial Neural Networks (ANNs) have always shown equivalent, and in many cases superior performance when compared to human physicians or conventional statistical methods. In recent years, SVM plays a dominant role in ANNs. The use of image information as input parameters to ANN models have also been shown to be efficient. These indicate that the incorporation of image analysis techniques into an ANN-based detection and progression of glaucoma is promising. Performance of ANNs is still not convincing enough. Supervised learning is used in all ANN models reported in this survey. Preparation of training and test data is crucial for the learning process and may influence the final outcome of the ANNs. When an ANN model is trained, factors such as inter- and intraobserver variability among pathologists, difference kinds of patients, different age groups and method of data collection may cause bias to the 'knowledge' learnt by the model and lead to inaccurate outcome. To overcome some of these shortcomings, a standardised validation procedure may be incorporated. A two level classifier has been chosen since the images are classified as affected or not affected by glaucoma. If the levels or degrees of severity of glaucoma has to be detected, then the classifiers may be extended to multi-level classifiers. Performance levels of ANNs can be increased by selecting the correct features to be given to the training set. The age of the patients chosen for training also has to be diverse to increase the accuracy of the training, which results in increased efficiency in the testing process. Both time and frequency domain features has to be incorporated to produce better results.

VIII. RETINAL DATABASES

There are several databases available. Some databases of retinal fundus images are available online. The most popular ones are STructured Analysis of the REtina(STARE) [27]. The STARE Project was conceived and initiated in 1975 by Michael Goldbaum, M.D., at the University of California, San Diego, and has been funded continuously by the National Institutes of Health (U.S.A.) since 1986. It also supports elaborate measurements of the anatomical structures and lesions visible in the retinal image. These measurements are useful for tracking disease severity and the evaluation of treatment progress over time. The STARE dataset has 31 images of healthy retinas and 50 images of pathological retinas which is widely used for benchmarking OD detection in the literature.The next most used database is the Digital Retinal Images for Vessel Extraction(DRIVE) [2]. The DRIVE database has been established to enable comparative studies on segmentation of blood vessels in retinal images. The photographs for the DRIVE database were obtained from a diabetic retinopathy screening program in The Netherlands. The screening population consisted of 400 diabetic subjects between $25 - 90$ years of age. Forty photographs have been randomly selected, 33 do not show any sign of diabetic retinopathy and 7 show signs of mild early diabetic retinopathy. Each image has been JPEG compressed. The set of 40 images has been divided into a training and a test set, both containing 20 images. For the training images, a single manual segmentation of the vasculature is available. For the test cases, two manual segmentations are available; one is used as gold standard, the other one can be used to compare computer generated segmentations with those of an independent human observer.

The ARIA project aims to provide an automated image capture and image analysis platform capable of predicting individuals at risk of eye disease. All photographs were taken at a 50 degree field width, and all images are in colour. Additionally, trained image analysis experts have traced out the blood vessels in the images and these are also given in sub-directories. It contains retinal images with manual outlines of vessels, OD and the location of the fovea. Another database in use is the Méthodes d'Evaluation de Systémes de Segmentation et d'Indexation Dédiées á l'Ophthalmologie Rétinienne (MESSIDOR). The MESSIDOR database has been established to facilitate studies on computer-assisted diagnoses of diabetic retinopathy. The 1200 eye fundus color

numerical images of the posterior pole for the MESSIDOR database were acquired by 3 ophthalmologic departments using a color video 3CCD camera on a Topcon TRC NW6 non-mydriatic retinograph with a 45 degree field of view. The images were captured using 8 bits per color plane at 1440 × 960, 2240 × 1488 or 2304 × 1536 pixels. The DIARETDB1 [13] is a standard Standard Diabetic Retinopathy Database for benchmarking diabetic retinopathy detection from digital images. The database consists of 89 colour fundus images of which 84 contain at least mild non-proliferative signs (Microaneurysms) of the diabetic retinopathy, and 5 are normal. Images were captured using the same 50 degree field-of-view digital fundus camera with varying imaging settings.

The Hamilton Eye Institute Macular Edema Dataset (HEI-MED) (formerly DMED) is a collection of 169 fundus images to train and test image processing algorithms for the detection of exudates and diabetic macular edema. The images have been collected as part of a telemedicine network for the diagnosis of diabetic retinopathy currently developed by the Hamilton Eye Institute, the Image Science and Machine Vision Group at Oak Ridge National Laboratory (ORNL) with the collaboration of the Université de Bourgogne. RIM-ONE is an online database with retinal fundus images and aims to be a reference for the design of ONH segmentation algorithms. RIM-ONE is exclusively focused on ONH segmentation, it has 169 high-resolution images and 5 manual reference segmentations and a gold standard of each one. The high number of expert segmentations enables the creation of reliable gold standards and the development of high accurate segmentation algorithms. ORIGA(-light) is an online retinal fundus image database for glaucoma analysis and research. Retinal fundus image is an important modality to document the health of the retina and is widely used to diagnose ocular diseases such as glaucoma, diabetic retinopathy and age-related macular degeneration.

IX. DISCUSSIONS AND CONCLUSIONS

The various computer technologies have helped the automation of detecting the OD accurately. A large number of researchers have reported on improved specificity and sensitivity in diagnosing glaucoma. A survey of those technologies [22], [34], [162], [163] has also been reported by various authors in analyzing the retinal image features. Machine intelligence technologies such as ANNs have helped the physicians in management and analysis of clinical data. When a neural network model is employed for medical image processing, compared with conventional image processing methods, there are several things that are to be considered. Firstly, the time for applying a trained neural network to solve a medical image processing problem is negligibly small, though the training of a neural network is a time consuming work. Secondly, medical image processing tasks often require complex computations. Hence the performance of ANNs can be significantly improved when image based information is added, which shows the need for (semi-)automatic segmentation and modelling. Moreover, in the diagnosis of diseases from functional images, computerised image processing technologies, when applied to, are time-efficient, reproducible and often more accurate than human experts. Among the reported localization algorithms, the Hough space determines the accurate ONH center and ROI and is seen to be more efficient. Segmentation of the ONH is determined accurately and precisely by Hu's circular model. Detection of glaucoma based on image analysis techniques has also been reported to be efficient. These technologies are expected to lead to improved diagnosis and treatment decision-making, and reduce the reliance on expensive and invasive diagnostic procedures.

Nevertheless, researchers must confront several great challenges. These cover all aspects of segmentation, classification and progression of glaucoma. In particular, the further development of statistical shape based segmentation techniques covering various modalities, registration of intra and inter modality data, and the inclusion of the surrounding anatomical structures and the potential information, might carry in an overall classification approach. These results should lead to a full 3-D model of the ONH including a probabilistic distribution of abnormalities and development of these over time. Finally, all this potential segmentation and classification information needs to be integrated into clinical evaluation tools of which ANNs are expected to remain the most logical choice (although SVM might challenge this dominance). Subsequent integration of the obtained information in the treatment process could be investigated.

Commercialisation and clinical application of computer technologies in the medical field require more reliable and comprehensive validation of these technologies. Currently, the role of computer-aided diagnosis in detection and progression of glaucoma have not yet been fully assessed and should be considered as an important complement to the physician's professional knowledge and judgment in making decisions. Besides the ongoing investigation of the technologies to improve their accuracy and robustness, substantial efforts should be put into the evaluation and validation of these technologies. To conclude, in the past decades, great efforts have been made to develop and apply computer technologies in clinical medicine, such as the detection of glaucoma, and as this research trend continues, the succeeding decades are likely to harvest the fruit of these efforts.

REFERENCES

[1] I. Akram and A. Rubinstein, "Common retinal signs. An overview," Optometry Today, Jan. 28, 2005. [Online]. Available: https://www.aop.org.uk/

[2] J. Staal, M. D. Abràmoff, M. Niemeijer, M. A. Viergever, and B. van Ginneken, "Ridge-based vessel segmentation in color images of the retina," *IEEE Trans. Med. Imag.*, vol. 23, no. 4, pp. 501–509, Apr. 2004.

[3] V. Grau, J. C. Downs, and C. F. Burgoyne, "Segmentation of trabeculated structures using an anisotropic Markov random field: Application to the study of the optic nerve head in glaucoma," *IEEE Trans. Med. Imag.*, vol. 25, no. 3, pp. 245–255, Mar. 2006.

[4] H. A. Quigley and A. T. Broman, "The number of people with glaucoma worldwide in 2010 and 2020," *Brit. J. Ophthalmol.*, vol. 90, pp. 262–267, Mar. 2006.

[5] F. Fumero, S. Alayon, J. L. Sanchez, J. Sigut, and M. Gonzalez-Hernandez, "RIM-ONE: An open retinal image database for optic nerve evaluation," in *Proc. 24th Int. Symp. Comput.-Based Med. Syst.*, 2011, pp. 1–6.

[6] F. A. Medeiros, L. M. Zangwill, C. Bowd, and R. N. Weinreb, "Comparison of the GDx VCC scanning laser polarimeter, HRT II confocalscanning laser ophthalmoscope, and stratus oct optical coherence tomographfor the detection of glaucoma," *Arch. Opthalmol.*, vol. 122, pp. 827–837, Jun. 2004.

[7] P. Naithani *et al.*, "Evaluation of optical coherence tomography and Heidelberg retinal tomography parameters in detecting early and moderate glaucoma," *Invest. Ophthalmol. Vis. Sci.*, vol. 48, pp. 3138–3145, Jul. 2007.

[8] L. M. Ventura, N. Sorokac, R. De Los Santos, W. J. Feuer, and V. Porciatti, "The relationship between retinal ganglion cell function and retinal nerve fiber thickness in early glaucoma," *Invest. Ophthalmol. Vis. Sci.*, vol. 47, pp. 3904–3911, Sep. 2006.

[9] J. B. Jonas, J. Stürmer, K. I. Papastathopoulos, F. Meier-Gibbons, and A. Dichtl, "Optic disc size and optic nerve damage in normal pressure glaucoma," *Brit. J. Ophthalmol.*, vol. 79, pp. 1102–1105, Aug. 1995.

[10] R. S. Harwerth and H. A. Quigley, "Visual field defects and retinal ganglion cell losses in patients with glaucoma," *Arch. Opthalmol.*, vol. 124, pp. 853–859, Jun. 2006.

[11] A. Sommer, I. Pollack, and A. E. Maumenee, "Optic disc parameters and onset of glaucomatous field loss. I. Methods and progressive changes in disc morphology," *Arch. Opthalmol.*, vol. 97, pp. 1444–1448, Aug. 1979.

[12] M. D. Abràmoff, M. K. Garvin, and M. Sonka, "Retinal imaging and image analysis," *IEEE Rev. Biomed. Eng.*, vol. 3, pp. 169–208, Dec. 2010.

[13] T. Kauppi *et al.*, "DIARETDB0: Evaluation database and methodology for diabetic retinopathy algorithms," Mach. Vis. Pattern Recognit. Res. Group, Lappeenranta Univ. Technol., Finland, 2006, pp. 1–17.

[14] G. Quellec, M. Lamard, P. M. Josselin, G. Cazuguel, B. Cochener, and C. Roux, "Optimal wavelet transform for the detection of microaneurysms in retina photographs," *IEEE Trans. Med. Imag.*, vol. 27, no. 9, pp. 1230–1241, Sep. 2008.

[15] A. Martidis *et al.*, "Intravitreal triamcinolone for refractory diabetic macular edema," *Ophthalmology*, vol. 109, no. 5, pp. 920–927, 2002.

[16] R. D. Jager, W. F. Mieler, and J. M. Miller, "Age-related macular degeneration," *New England J. Med.*, vol. 358, no. 24, pp. 2606–2617, 2008.

[17] VisionAware. *Age-Related Macular Degeneration (AMD)—Vision Aware, Self Help for Vision Loss*, accessed on Jan. 15, 2016. [Online]. Available: http://www.visionaware.org

[18] R. Klein, T. Peto, A. Bird, and M. R. Vannewkirk, "The epidemiology of age-related macular degeneration," *Amer. J. Ophthalmol.*, vol. 137, no. 3, pp. 486–495, 2004.

[19] L. S. Lim, P. Mitchell, J. M. Seddon, F. G. Holz, and T. Y. Wong, "Age-related macular degeneration," *Lancet*, vol. 379, no. 9827, pp. 1728–1738, 2012.

[20] C.-L. Tsai *et al.*, "Automated retinal image analysis over the internet," *IEEE Trans. Inf. Technol. Biomed.*, vol. 12, no. 4, pp. 480–487, Jul. 2008.

[21] I. N. Bankman, Ed., *Handbook of Medical Image Processing and Analysis*. Baltimore, MD, USA: The Johns Hopkins Univ. Press, 2000, pp. 1084–1098.

[22] S. R. Nirmala, M. K. Nath, and S. Dandapat, "Retinal image analysis: A review," *Int. J. Comput. Commun. Technol.*, vol. 2, pp. 11–15, Jul. 2011.

[23] H. Narasimha-Iyer, B. R. Ali Can, H. L. Tanenbaum, and A. Majerovics, "Integrated analysis of vascular and nonvascular changes from color retinal fundus image sequences," *IEEE Trans. Biomed. Eng.*, vol. 54, no. 8, pp. 1436–1445, Aug. 2007.

[24] L. G. Nyúl, "Retinal image analysis for automated glaucoma risk evaluation," *Proc. SPIE*, vol. 7497, pp. 891–899, Sep. 2009.

[25] H. Yu *et al.*, "Fast localization and segmentation of optic disk in retinal images using directional matched filtering and level sets," *IEEE Trans. Inf. Technol. Biomed.*, vol. 16, no. 4, pp. 644–657, Jul. 2012.

[26] S. Y. Lee *et al.*, "Automated quantification of retinal nerve fiber layer atrophy in fundus photograph," in *Proc. 26th Annu. Int. Conf. IEEE EMBS*, Sep. 2004, pp. 1241–1243.

[27] D. Santhi, S. Karkuzhali, and D. Manimegalai, "Locating optic disc center and segmenting blood vessels in retinal images for screening system of diabetic retinopathy," *Int. J. Res. Rev. Inf. Technol.*, vol. 1, pp. 20–27, Mar. 2011.

[28] R. C. Gonzalez, *Digital Image Processing*. New Delhi, India: Prentice-Hall, 2002, pp. 461–475.

[29] S. K. Kim *et al.*, "Segmentation of optic nerve head using warping and RANSAC," in *Proc. 29th Annu. Int. Conf. IEEE EMBS*, Aug. 2007, pp. 900–903.

[30] M. C. V. S. Mary, E. B. Rajsingh, J. K. K. Jacob, D. Anandhi, U. Amato, and S. E. Selvan, "An empirical study on optic disc segmentation using an active contour model," *Biomed. Signal Process. Control*, vol. 18, pp. 19–29, Apr. 2014.

[31] A. Salazar-Gonzalez, D. Kaba, Y. Li, and X. Liu, "Segmentation of the blood vessels and optic disk in retinal images," *IEEE J. Biomed. Health Informat.*, vol. 18, no. 6, pp. 1874–1886, Nov. 2014.

[32] H. Wang, W. Hsu, K. G. Goh, and M. L. Lee, "An effective approach to detect lesions in color retinal images," in *Proc. IEEE Conf. Comput. Vis. Pattern Recognit.*, Jun. 2000, pp. 181–186.

[33] C. Eswaran, A. W. Reza, and S. Hati, "Extraction of the contours of optic disc and exudates based on marker-controlled watershed segmentation," in *Proc. Int. Conf. Comput. Sci. Inf. Technol.*, 2008, pp. 719–723.

[34] M. Balasubramanian, C. Bowd, and L. M. Zangwill, "Algorithms for detecting glaucomatous structural changes in the optic nerve head," *Image Model. Human Eye*, vol. 1, pp. 11–15, Apr. 2008.

[35] R. Chrástek *et al.*, "Automated segmentation of the optic nerve head for diagnosis of glaucoma," *Med. Image Anal.*, vol. 9, pp. 297–314, Aug. 2005.

[36] A. Youssif, A. Z. Ghalwash, and A. S. Ghoneim, "A comparative evaluation of preprocessing methods for automatic detection of retinal anatomy," in *Proc. 5th Int. Conf. Inf. Syst. (INFOS)*, vol. 5. Mar. 2007, pp. 461–475.

[37] B. Dashtbozorg, A. M. Mendonça, and A. Campilho, "Optic disc segmentation using the sliding band filter," *Comput. Biol. Med.*, vol. 61, pp. 2112–2124, Oct. 2014.

[38] V. Murray, M. Pattichis, and P. Soliz, "New AM-FM analysis methods for retinal image characterization," in *Proc. 42nd Asilomar Conf. Signals, Syst. Comput.*, Oct. 2008, pp. 664–668.

[39] S. Sekhar, W. Al-Nuaimy, and A. K. Nandi, "Automated localisation of optic disk and fovea in retinal fundus images," in *Proc. EUSIPCO*, Aug. 2008, pp. 1–5.

[40] A. Osareh, M. Mirmehdi, B. Thomas, and R. Markham, "Comparison of colour spaces for optic disc localisation in retinal images," in *Proc. 16th Int. Conf. Pattern Recognit. (ICPR)*, Aug. 2002, pp. 743–746.

[41] S. Samanta, S. K. Saha, and B. Chanda, "A simple and fast algorithm to detect the fovea region in fundus retinal image," in *Proc. 2nd Int. Conf. Emerg. Appl. Inf. Technol.*, Feb. 2011, pp. 206–209.

[42] A. Osareh, M. Mirmehdi, B. Thomas, and R. Markhamb, "Colour morphology and snakes for optic disc localisation," in *Proc. 6th Med. Image Understand. Anal. Conf.*, Jul. 2002, pp. 21–24.

[43] H. Narasimha-Iyer *et al.*, "Robust detection and classification of longitudinal changes in color retinal fundus images for monitoring diabetic retinopathy," *IEEE Trans. Biomed. Eng.*, vol. 53, no. 6, pp. 1084–1098, Jun. 2006.

[44] C. Sinthanayothin, J. F. Boyce, H. L. Cook, and T. H. Williamson, "Automated localisation of the optic disc, fovea, and retinal blood vessels from digital colour fundus images," *Brit. J. Opthalmol*, vol. 16, pp. 902–910, Aug. 2002.

[45] S. Morales, V. Naranjo, J. Angulo, and M. Alcañiz, "Automatic detection of optic disc based on PCA and mathematical morphology," *IEEE Trans. Med. Imag.*, vol. 32, no. 4, pp. 786–796, Apr. 2013.

[46] A. A.-H. A.-R. Youssif, A. Ghalwash, A. A. Sabry, and A.-R. Ghoneim, "Optic disc detection from normalized digital fundus images by means of a vessels' direction matched filter," *IEEE Trans. Med. Imag.*, vol. 27, no. 1, pp. 11–18, Jan. 2008.

[47] H. Cao, B. Khoobehi, and S. S. Iyengar, "Automated optic nerve head image fusion of nonhuman primate eyes using heuristic optimization algorithm," in *Proc. IEEE Symp. Comput. Intell. Bioinform. Comput. Biol. (CIBCB)*, Sep. 2008, pp. 228–232.

[48] N. Otsu, "A threshold selection method from gray-level histograms," *IEEE Trans. Syst., Man, Cybern.*, vol. 9, no. 1, pp. 62–66, Jan. 1979.

[49] X. Yang, P. Morrow, and B. Scotney, "Optic nerve head segmentation in HRT images," in *Proc. IEEE Int. Conf. Image Process.*, Oct. 2006, pp. 65–68.

[50] S.-C. Cheng and Y.-M. Huang, "A novel approach to diagnose diabetes based on the fractal characteristics of retinal images," *IEEE Trans. Inf. Technol. Biomed.*, vol. 7, no. 3, pp. 163–170, Sep. 2003.

[51] S. S. Leel, M. Rajeswari, and D. Ramachandram, "Preliminary and multi features localisation of optic disc in colour fundus images," in *Proc. National Comput. Sci. Postgraduate Colloq.*, 2005, pp. 1–5.
[52] R. Chrastek, M. Wolf, K. Donath, G. Michelson, and H. Niemann, "Optic disc segmentation in retinal images," in *Proc. Bavarian Res. Center Knowl. Syst.*, 2006, pp. 263–266.
[53] J. Liu *et al.*, "Optic cup and disk extraction from retinal fundus images for determination of cup-to-disc ratio," in *Proc. 3rd IEEE Conf. Ind. Electron. Appl.*, Jun. 2008, pp. 1828–1832.
[54] H. Li and O. Chutatape, "Automatic location of optic disk in retinal images," in *Proc. Int. Conf. Image Process.*, vol. 2. Oct. 2001, pp. 837–840.
[55] K. Noronha, J. Nayak, and S. N. Bhat, "Enhancement of retinal fundus image to highlight the features for detection of abnormal eyes," in *Proc. IEEE Region 10 Conf. (TENCON)*, Nov. 2006, pp. 1–4.
[56] T. B. Tang, C. K. Lu, A. Laude, B. Dhillon, and A. F. Murray, "Noise reduction for ellipse fitting on medical images," *Electron. Lett.*, vol. 49, no. 3, pp. 178–179, Jan. 2013.
[57] S. Roychowdhury, D. D. Koozekanani, S. N. Kuchinka, and K. K. Parhi, "Optic disc boundary and vessel origin segmentation of fundus images," *IEEE J. Biomed. Health Informat.*, Aug. 2015.
[58] P. C. Siddalingaswamy and K. G. Prabhu, "Automatic localization and boundary detection of optic disc using implicit active contours," *Int. J. Comput. Appl.*, vol. 1, no. 7, pp. 1–5, 2010.
[59] M. Lalonde, M. Beaulieu, and L. Gagnon, "Fast and robust optic disc detection using pyramidal decomposition and Hausdorff-based template matching," *IEEE Trans. Med. Imag.*, vol. 20, no. 11, pp. 1193–1200, Nov. 2001.
[60] B. Harangi, R. J. Qureshi, A. Csutak, T. Peto, and A. Hajdu, "Automatic detection of the optic disc using majority voting in a collection of optic disc detectors," in *Proc. IEEE Int. Symp. Biomed. Imag., Nano Macro*, Apr. 2010, pp. 1329–1332.
[61] L. Kovacs, R. J. Qureshi, B. Nagy, B. Harangi, and A. Hajdu, "Graph based detection of optic disc and fovea in retinal images," in *Proc. 4th Int. Workshop Soft Comput. Appl. (SOFA)*, Jul. 2010, pp. 143–148.
[62] K. A. Goatman, A. D. Fleming, S. Philip, G. J. Williams, J. A. Olson, and P. F. Sharp, "Detection of new vessels on the optic disc using retinal photographs," *IEEE Trans. Med. Imag.*, vol. 30, no. 4, pp. 972–979, Feb. 2011.
[63] N. Inoue, K. Yanashima, K. Magatani, and T. Kurihara, "Development of a simple diagnostic method for the glaucoma using ocular fundus pictures," in *Proc. 27th Annu. Conf. IEEE Eng. Med. Biol.*, Sep. 2005, pp. 3355–3358.
[64] E. Corona, S. Mitra, M. Wilson, T. Krile, Y. H. Kwon, and P. Soliz, "Digital stereo image analyzer for generating automated 3-D measures of optic disc deformation in glaucoma," *IEEE Trans. Med. Imag.*, vol. 21, no. 10, pp. 1244–1253, Oct. 2002.
[65] P. L. Rosin, D. Marshall, and J. E. Morgan, "Multimodal retinal imaging: New strategies for the detection of glaucoma," in *Proc. Int. Conf. Image Process.*, vol. 3. 2002, pp. 137–140.
[66] T. Walter and J.-C. Klein, "Segmentation of color fundus images of the human retina: Detection of the optic disc and the vascular tree using morphological techniques," in *Proc. 2nd Int. Symp. Med. Data Anal.*, 2001, pp. 282–287.
[67] D. Zhang and Y. Zhao, "Novel accurate and fast optic disc detection in retinal images with vessel distribution and directional characteristics," *IEEE J. Biomed. Health Informat.*, vol. 20, no. 1, pp. 333–342, Jan. 2016.
[68] L. Gagnon, M. Lalonde, M. Beaulieu, and M. C. Boucher, "Procedure to detect anatomical structures in optical fundus images," *Proc. SPIE*, vol. 4322, pp. 1218–1225, Jul. 2001.
[69] H. Li and O. Chutatape, "Automated feature extraction in color retinal images by a model based approach," *IEEE Trans. Biomed. Eng.*, vol. 51, no. 2, pp. 246–254, Feb. 2004.
[70] A. V. Sagar, S. Balasubramanian, and V. Chandrasekaran, "Automatic detection of anatomical structures in digital fundus retinal images," in *Proc. IAPR Conf. Mach. Vis. Appl. (MVA)*, May 2007, pp. 164–168.
[71] D. Koozekanani, K. L. Boyer, and C. Roberts, "Tracking the optic nervehead in oct video using dual eigenspaces and an adaptive vascular distribution model," *IEEE Trans. Med. Imag.*, vol. 22, no. 12, pp. 1519–1536, Dec. 2003.
[72] T. P. Karnowski, V. P. Govindasamy, K. W. Tobin, and E. Chaum, "Locating the optic nerve in retinal images: Comparing model-based and Bayesian decision methods," in *Proc. Conf. IEEE Eng. Med. Biol. Soc.*, Aug./Sep. 2006, pp. 4436–4439.
[73] R. Zhu, M. Rangayyan, and A. L. Ells, "Detection of the optic nerve head in fundus images of the retina using the hough transform for circles," *J. Digit. Imag. Soc. Imag. Inform. Med.*, vol. 23, no. 3, pp. 332–341, Feb. 2009.
[74] R. A. Abdel-Ghafar and T. Morris, "Progress towards automated detection and characterization of the optic disc in glaucoma and diabetic retinopathy," *Med. Inform. Internet Med.*, vol. 32, pp. 19–25, Mar. 2007.
[75] R. A. Abdel-Ghafar, T. Morris, T. Ritchings, and I. Wood, "Detection and characterisation of the optic disk in glaucoma and diabetic retinopathy," Ph.D. dissertation, Dept. Comput. School Comput., Sci. Eng., UMIST, Manchester, U.K., Jan. 2007.
[76] P. Treigys, V. Šaltenis, G. Dzemyda, V. Barzdžiukas, and A. Paunksnis, "Automated optic nerve disc parameterization," *Informatica*, vol. 19, pp. 403–420, Mar. 2008.
[77] A. Aquino, M. E. Gegúndez, and D. Marín, "Automated optic disc detection in retinal images of patients with diabetic retinopathy and risk of macular edema," *Int. J. Biol. Life Sci.*, vol. 8, p. 87, Feb. 2012.
[78] A. Pinz, S. Bernogger, P. Datlinger, and A. Kruger, "Mapping the human retina," *IEEE Trans. Med. Imag.*, vol. 17, no. 4, pp. 606–619, Aug. 1998.
[79] R. O. Duda and R. E. Hart, "Use of the Hough transformation to detect lines and curves in pictures," *Commun. ACM*, vol. 15, no. 1, pp. 11–15, Jan. 1972.
[80] G. D. Joshi, J. Sivaswamy, and S. R. Krishnadas, "Optic disk and cup segmentation from monocular color retinal images for glaucoma assessment," *IEEE Trans. Med. Imag.*, vol. 30, no. 6, pp. 1192–1205, Jun. 2011.
[81] A. Aquino, M. Emilio, E. Gegundez-Arias, and D. Marin, "Detecting the optic disc boundary in digital fundus images using morphological, edge detection, and feature extraction techniques," *IEEE Trans. Med. Imag.*, vol. 29, no. 11, pp. 1860–1869, Nov. 2010.
[82] N. H. Solouma, A.-B. M. Youssef, Y. A. Badr, and Y. M. Kadah, "A new real-time retinal tracking system for image-guided laser treatment," *IEEE Trans. Biomed. Eng.*, vol. 49, no. 9, pp. 1059–1067, Sep. 2002.
[83] M. S. Mabrouk, N. H. Solouma, and Y. M. Kadah, "Survey of retinal image segmentation and registration," *GVIP J.*, vol. 6, pp. 1–11, Sep. 2006.
[84] D. Marina, M. E. Gegundez-Ariasb, A. Sueroa, and J. M. Bravo, "Obtaining optic disc center and pixel region by automatic thresholding methods on morphologically processed fundus images," *Comput. Programs Methods Biomed.*, vol. 118, pp. 173–185, Dec. 2014.
[85] S. Lu and J. H. Lim, "Automatic optic disc detection from retinal images by a line operator," *IEEE Trans. Biomed. Eng.*, vol. 58, no. 1, pp. 88–94, Jan. 2011.
[86] S. Lu, "Accurate and efficient optic disc detection and segmentation by a circular transformation," *IEEE Trans. Med. Imag.*, vol. 30, no. 12, pp. 2126–2133, Dec. 2011.
[87] S. Lu and J. H. Lim, "Automatic macula detection from retinal images by a line operator," in *Proc. IEEE 17th Int. Conf. Image Process.*, Sep. 2010, pp. 4073–4076.
[88] J. Lowell *et al.*, "Optic nerve head segmentation," *IEEE Trans. Med. Imag.*, vol. 23, no. 2, pp. 256–264, Feb. 2004.
[89] S. P. C. Marino, M. G. Penedo, M. Ortega, J. Rouco, A. Pose-Reino, and M. Pena, "Macula precise localization using digital retinal angiographies," *WSEAS Trans. Comput. Res.*, vol. 3, pp. 43–50, Jan. 2008.
[90] C. Mariño *et al.*, "Optic disc segmentation using a matching filter and a deformable model," in *Proc. 6th WSEAS Int. Conf. Appl. Comput. Sci.*, Tenerife, Spain, Dec. 2006, pp. 207–213.
[91] M. Foracchia, E. Grisan, and A. Ruggeri, "Detection of optic disc in retinal images by means of a geometrical model of vessel structure," *IEEE Trans. Med. Imag.*, vol. 23, no. 10, pp. 1189–1195, Oct. 2004.
[92] H. F. Jelinek, C. Depardieu, C. Lucas, D. J. Cornforth, W. Huang, and M. J. Cree, "Towards vessel characterisation in the vicinity of the optic disc in digital retinal images," in *Proc. Int. Conf. Image Vis. Comput. New Zealand (IVCNZ)*, 2005, pp. 2–7.
[93] M. Niemeijer, M. D. Abràmoff, and B. van Ginneken, "Segmentation of the optic disc, macula and vascular arch in fundus photographs," *IEEE Trans. Med. Imag.*, vol. 26, no. 1, pp. 116–127, Jan. 2007.
[94] M. Niemeijer, B. van Ginneken, F. ter Haar, and M. D. Abràmoff, "Automatic detection of the optic disc, fovea and vascular arch in digital color photographs of the retina," in *Proc. Brit. Mach. Vis. Conf.*, 2005, pp. 109–118.

[95] D. Koozekanani, K. L. Boyer, and C. Roberts, "Tracking the optic nervehead in OCT video using dual eigenspaces and an adaptive vascular distribution model," *IEEE Trans. Med. Imag.*, vol. 22, no. 12, pp. 1519–1536, Dec. 2003.

[96] N. M. Tan, J. Liu, D. W. K. Wong, F. Yin, J. H. Lim, and T. Y. Wong, "Mixture model-based approach for optic cup segmentation," in *Proc. 32nd Annu. Int. Conf. IEEE EMBS Buenos Aires*, Aug./Sep. 2010, pp. 4817–4820.

[97] S. Yousefi *et al.*, "Learning from data: Recognizing glaucomatous defect patterns and detecting progression from visual field measurements," *IEEE Trans. Biomed. Eng.*, vol. 61, no. 7, pp. 2112–2124, Jul. 2014.

[98] P. Radeva, J. Serrat, and E. Marti, "A snake for model-based segmentation," in *Proc. 5th Int. Conf. Comput. Vis.*, vol. 7. Jun. 1995, pp. 816–821.

[99] C. H. Esteban and F. Schmitt, "A snake approach for high quality image-based 3d object modeling," in *Variational, Geometric and Level Set Methods in Computer Vision*, 2003, pp. 241–248.

[100] D. L. Pham, C. Xu, and J. L. Prince, "Current methods in medical image segmentation," *Annu. Rev. Biomed. Eng.*, vol. 2, pp. 315–337, Jul. 2000.

[101] M. Kass, A. Witkin, and D. Terzopoulos, "Snakes: Active contour models," in *Proc. 1st Int. Conf. Comput. Vis.*, vol. 1. London, U.K., 1987, pp. 259–267.

[102] M. Bakoš, "Active contours and their utilization at image segmentation," in *Proc. 5th Slovakian-Hungarian Joint Symp. Appl. Mach. Intell. Inform.*, Jan. 2007, pp. 313–317.

[103] F. Mendels, C. Heneghan, and J. P. Thiran, "Identification of the optic disk boundary in retinal images using active contours," in *Proc. Irish Mach. Vis. Image Process. Conf.*, 1999, pp. 103–115.

[104] M. Burger and S. J. Osher, "A survey on level set methods for inverse problems and optimal design," *Eur. J. Appl. Math.*, vol. 16, no. 2, pp. 263–301, 2004.

[105] C. Xu, A. Yezzi, and J. L. Prince, "A summary of geometric level-set analogues for a general class of parametric active contour and surface models," in *Proc. 1st IEEE Workshop Variational Level Set Methods Comput. Vis.*, 2001, pp. 104–111.

[106] X. Han, C. Xu, and J. L. Prince, "A topology preserving level set method for geometric deformable models," *IEEE Trans. Pattern Anal. Mach. Intell.*, vol. 25, no. 6, pp. 755–768, Jun. 2003.

[107] Y. Tang, X. Li, A. von Freyberg, and G. Goch, "Automatic segmentation of the papilla in a fundus image based on the C-V model and a shape restraint," in *Proc. 18th Int. Conf. Pattern Recognit.*, vol. 1. 2006, pp. 183–186.

[108] A. R. Hussain, "Optic nerve head segmentation using genetic active contours," in *Proc. Int. Conf. Comput. Commun. Eng.*, May 2008, pp. 783–787.

[109] C. Xu and J. L. Prince, "Global optimality of gradient vector flow," in *Proc. 34th Annu. Conf. Inf. Sci. Syst.*, Mar. 2000, pp. 15–17.

[110] M. Balasubramanian *et al.*, "A framework for detecting glaucomatous progression in the optic nerve head of an eye using proper orthogonal decomposition," *IEEE Trans. Inf. Technol. Biomed.*, vol. 13, no. 5, pp. 781–793, Sep. 2009.

[111] A. J. Patterson, D. F. Garway-Heath, N. G. Strouthidis, and D. P. Crabb, "A new statistical approach for quantifying change in series of retinal and optic nerve head topography images," *Invest. Ophthalmol. Vis. Sci.*, vol. 46, pp. 1659–1667, May 2005.

[112] N. O. Leary *et al.*, "Glaucomatous progression in series of stereoscopic photographs and Heidelberg retina tomograph images," *Arch. Ophthalmol.*, vol. 128, pp. 560–568, May 2010.

[113] M. Balasubramanian *et al.*, "Clinical evaluation of the proper orthogonal decomposition framework for detecting glaucomatous changes in human subjects," *Invest. Ophthalmol. Vis. Sci.*, vol. 51, pp. 264–271, Jan. 2010.

[114] A. Poli, N. G. Strouthidis, T. A. Ho, and D. F. Garway-Heath, "Analysis of HRT images: Comparison of reference planes," *Invest. Ophthalmol. Vis. Sci.*, vol. 49, pp. 3970–3975, Sep. 2008.

[115] J. Cheng *et al.*, "Superpixel classification based optic disc and optic cup segmentation for glaucoma screening," *IEEE Trans. Med. Imag.*, vol. 32, no. 6, pp. 1019–1032, Jun. 2013.

[116] A. A. Vlachokosta, P. A. Asvestas, G. K. Matsopoulos, N. Uzunoglu, and T. G. Zeyen, "Preliminary study on the association of vessel diameter variation and glaucoma," in *Proc. 29th Annu. Int. Conf. IEEE EMBS*, Aug. 2007, pp. 888–891.

[117] D. C. DeBuc, "A review of algorithms for segmentation of retinal image data using optical coherence tomography," in *Image Segmentation*. Croatia: INTECH, Apr. 2011, pp. 15–54.

[118] A. Herzog, K. L. Boyer, and C. Roberts, "Extracting the optic disk endpoints in optical coherence tomography data," in *Proc. 7th IEEE Workshop Appl. Comput. Vis.*, Jan. 2005, pp. 263–268.

[119] J. Xu, H. Ishikawa, G. Wollstein, L. Kagemann, and J. S. Schuman, "Alignment of 3-D optical coherence tomography scans to correct eye movement using a particle filtering," *IEEE Trans. Med. Imag.*, vol. 31, no. 7, pp. 1337–1345, Jul. 2012.

[120] M. S. Miri *et al.*, "Multimodal segmentation of optic disc and cup from SD-OCT and color fundus photographs using a machine-learning graph-based approach," *IEEE Trans. Med. Imag.*, vol. 34, no. 9, pp. 1854–1866, Sep. 2015.

[121] M. D. Abràmoff *et al.*, "Automated segmentation of the cup and rim from spectral domain OCT of the optic nerve head," *Invest. Ophthalmol. Vis. Sci.*, vol. 50, pp. 5778–5784, Dec. 2009.

[122] C. K. Leung *et al.*, "Analysis of retinal nerve fiber layer and optic nerve head in glaucoma with different reference plane offsets, using optical coherence tomography," *Invest. Ophthalmol. Vis. Sci.*, vol. 46, pp. 891–899, Mar. 2005.

[123] C. Bowd *et al.*, "Detecting early glaucoma by assessment of retinal nerve fiber layer thickness and visual function," *Invest. Ophthalmol. Vis. Sci.*, vol. 42, pp. 1993–2003, Aug. 2001.

[124] M. Dias, V. Vidotti, V. P. Costa, and E. S. Gomi, "High definition optical coherence tomography and standard automated perimetry dataset generator for glaucoma diagnosis," in *Proc. 1st Annu. ORNL Biomed. Sci. Eng. Conf.*, Mar. 2009, pp. 1–4.

[125] S. Yousefi *et al.*, "Glaucoma progression detection using structural retinal nerve fiber layer measurements and functional visual field points," *IEEE Trans. Med. Imag.*, vol. 61, no. 4, pp. 1143–1154, Apr. 2014.

[126] K. R. Sung, J. H. Sun, J. H. Na, J. Y. Lee, and Y. Lee, "Progression detection capability of macular thickness in advanced glaucomatous eyes," *Amer. Acad. Ophthalmol.*, vol. 119, no. 2, pp. 308–313, Feb. 2012.

[127] J.-C. Mwanza *et al.*, "Glaucoma diagnostic accuracy of ganglion cell-inner plexiform layer thickness: Comparison with nerve fiber layer and optic nerve head," *Amer. Acad. Ophthalmol.*, vol. 119, pp. 1151–1158, Jun. 2012.

[128] H. Akiyama, T. Kashima, D. Li, Y. Shimoda, R. Mukai, and S. Kishi, "Retinal ganglion cell analysis in Leber's hereditary optic neuropathy," *Ophthalmology*, vol. 120, pp. 1943–1944, Sep. 2013.

[129] N. V. Swindale, G. Stjepanovic, A. Chin, and F. S. Mikelberg, "Automated analysis of normal and glaucomatous optic nerve head topography images," *Invest. Ophthalmol. Vis. Sci.*, vol. 41, pp. 1730–1742, Jun. 2000.

[130] A. B. Cullinane, A. Waldock, J. P. Diamond, and J. M. Sparrow, "Optic disc cup slope and visual field indices in normal, ocular hypertensive and early glaucomatous eyes," *Brit. J. Ophthalmol.*, vol. 86, no. 5, pp. 555–559, 2002.

[131] L. A. Paunescu *et al.*, "Reproducibility of nerve fiber thickness, macular thickness, and optic nerve head measurements using StratusOCT," *Invest. Ophthalmol. Vis. Sci.*, vol. 45, pp. 1716–1724, Jun. 2004.

[132] H. Fu, D. Xu, S. Lin, D. W. K. Wong, and J. Liu, "Automatic optic disc detection in OCT slices via low-rank reconstruction," *IEEE Trans. Biomed. Eng.*, vol. 62, no. 4, pp. 1151–1158, Apr. 2015.

[133] S. Ramanathan and R. Balaraman, "Automatic detection of accretion of glaucoma in eye," in *Proc. 14th Int. Workshop Syst., Signals Image Process., 6th EURASIP Conf. Focused Speech Image Process., Multimedia Commun. Services*, Jun. 2007, pp. 441–445.

[134] F. Rossant, I. Ghorbel, I. Bloch, M. Paques, and S. Tick, "Automated segmentation of retinal layers in OCT imaging and derived ophthalmic measures," in *Proc. IEEE Int. Symp. Biomed. Imag.*, Jun./Jul. 2009, pp. 1370–1373.

[135] V. Grau, J. C. Downs, and C. F. Burgoyne, "Segmentation of connective tissue in the optic nerve head using an anisotropic Markov random field," in *Proc. IEEE Int. Symp. Biomed. Imag. Nano Macro*, vol. 1. Apr. 2004, pp. 93–96.

[136] K. L. Boyer, A. Herzog, and C. Roberts, "Automatic recovery of the optic nervehead geometry in optical coherence tomography," *IEEE Trans. Med. Imag.*, vol. 25, no. 5, pp. 553–570, May 2006.

[137] K. Lee, M. Niemeijer, M. K. Garvin, Y. H. Kwon, M. Sonka, and M. D. Abràmoff, "Segmentation of the optic disc in 3-D OCT scans of the optic nerve head," *IEEE Trans. Med. Imag.*, vol. 29, no. 1, pp. 159–168, Jan. 2010.

[138] M. D. Abràmoff *et al.*, "Automated segmentation of the optic disc from stereo color photographs using physiologically plausible features," *Invest. Ophthalmol. Vis. Sci.*, vol. 48, pp. 1665–1673, Apr. 2007.

[139] J.-M. Park, J. Reed, and Q. Zhou, "Active feature selection in optic nerve data using support vector machine," in *Proc. Int. Joint Conf. Neural Netw. (IJCNN)*, vol. 2. May 2002, pp. 1178–1182.
[140] S. H. Haykin, *Neural Networks: A Comprehensive Foundation*, 2nd ed. Englewood Cliffs, NJ, USA: Prentice-Hall, 1999.
[141] C. M. Bishop, *Neural Networks for Pattern Recognition*. Oxford, U.K.: Clarendon, 1995.
[142] K. Chan, T.-W. Lee, P. A. Sample, M. H. Goldbaum, R. N. Weinreb, and T. J. Sejnowski, "Comparison of machine learning and traditional classifiers in glaucoma diagnosis," *IEEE Trans. Biomed. Eng.*, vol. 49, no. 9, pp. 963–974, Sep. 2002.
[143] D. W. K. Wong *et al.*, "Intelligent fusion of cup-to-disc ratio determination methods for glaucoma detection in ARGALI," in *Proc. 31st Annu. Int. Conf. IEEE EMBS*, Minneapolis, MN, USA, Sep. 2009, pp. 5777–5780.
[144] C. J. C. Burges, "A tutorial on support vector machines for pattern recognition," in *Data Mining and Knowledge Discovery*. Boston, MA, USA: Kluwer, 1998, pp. 121–167.
[145] C.-W. Hsu, C.-C. Chang, and C.-J. Lin, "A practical guide to support vector classification," Dept. Comput. Sci., National Taiwan Univ., Taipei, Taiwan, Tech. Rep., 2010, pp. 1–16.
[146] D. K. Srivastava and L. Bhambhu, "Data classification using support vector machine," *J. Theor. Appl. Inf. Technol.*, vol. 1, no. 10, pp. 185–189, 2009.
[147] M.-L. Huang, H.-Y. Chen, W.-C. Huang, and Y.-Y. Tsai, "Linear discriminant analysis and artificial neural network for glaucoma diagnosis using scanning laser polarimetry-variable cornea compensation measurements in Taiwan Chinese population," *Graefes Arch. Clin. Exp. Ophthalmol.*, vol. 248, no. 3, pp. 435–441, 2010.
[148] A. Peters, B. Lausen, G. Michelson, and O. Gefeller, "Diagnosis of glaucoma by indirect classifiers," *Methods Inf. Med.*, vol. 42, no. 1, pp. 99–103, 2003.
[149] S. von Spreckelsen, P. Grumstup, J. Johnsen, and L. K. Hansen, "Modeling of glaucoma induced changes in the retina and neural net assisted diagnosis," in *Proc. IEEE Workshop Neural Netw. Signal Process.*, Sep. 1994, pp. 490–498.
[150] C. M. Pditt, F. S. Mikelberg, and N. V. Swindale, "The detection of glaucoma using an artificial neural network," in *Proc. IEEE 17th Annu. Conf. Eng. Med. Biol. Soc.*, vol. 1. Sep. 1995, pp. 847–848.
[151] M. J. Greaney, D. C. Hoffman, D. F. Garway-Heath, M. Nakla, A. L. Coleman, and J. Caprioli, "Comparison of optic nerve imaging methods to distinguish normal eyes from those with glaucoma," *Invest. Ophthalmol. Vis. Sci.*, vol. 43, pp. 140–145, Jan. 2002.
[152] K. W. Tobin, E. Chaum, V. P. Govindasamy, and T. P. Karnowski, "Detection of anatomic structures in human retinal imagery," *IEEE Trans. Med. Imag.*, vol. 26, no. 12, pp. 1729–1739, Dec. 2011.
[153] K. W. Tobin, E. Chaum, V. P. Govindasamy, T. P. Karnowski, and O. Sezer, "Characterization of the optic disc in retinal imagery using a probabilistic approach," *Proc. SPIE*, vol. 6144, p. 61443F, Mar. 2006.
[154] J. E. Pederson and D. R. Anderson, "The mode of progressive disc cupping in ocular hypertension and glaucoma," *Arch. Opthalmol.*, vol. 98, pp. 490–495, Mar. 1980.
[155] R. A. Hitchings, "The optic disc in glaucoma, III: Diffuse optic disc pallor with raised intraocular pressure," *Brit. J. Ophthalmol.*, vol. 62, no. 10, pp. 670–675, 1978.
[156] J. Xu *et al.*, "Automated assessment of the optic nerve head on stereo disc photographs," *Invest. Ophthalmol. Vis. Sci.*, vol. 49, pp. 2512–2517, Jun. 2008.
[157] J. Xu, O. Chutatape, C. Zheng, and P. C. T. Kuan, "Three dimensional optic disc visualisation from stereo images via dual registration and ocular media optical correction," *Brit. J. Ophthalmol.*, vol. 90, pp. 181–185, Feb. 2006.
[158] H. J. Kong *et al.*, "Three dimensional reconstruction of conventional stereo optic disc image," in *Proc. 26th Annu. Int. Conf. IEEE EMBS*, Sep. 2004, pp. 1229–1232.
[159] J. Yu, S. S. R. Abidi, P. H. Artes, A. McIntyre, and M. Heywood, "Automated optic nerve analysis for diagnostic support in glaucoma," in *Proc. 18th IEEE Symp. Comput.-Based Med. Syst.*, Jun. 2005, pp. 97–102.
[160] Y. V. Vorobyev, *Method of Moments in Applied Mathematics*. New York, NY, USA: Gordon Breach Sci. Pub., 1965.
[161] G. Zahlmonn, M. Stherf, A. Wegner, M. Obermoier, and M. Mertz, "Situation assessment of glaucoma using a hybrid fuzzy neural network," *IEEE Eng. Med. Biol.*, vol. 19, no. 1, pp. 84–91, Jan./Feb. 2000.
[162] J. Anitha, C. K. S. Vijila, and D. J. Hemanth, "An overview of computational intelligence techniques for retinal disease identification applications," *Int. J. Rev. Comput.*, vol. 5, pp. 29–46, Jan. 2011.
[163] N. Patton *et al.*, "Retinal image analysis: Concepts, applications and potential," *Prog. Retinal Eye Res.*, vol. 25, pp. 99–127, Jan. 2006.

M. CAROLINE VIOLA STELLA MARY received the B.E. degree in electronics and communication engineering from the Government College of Engineering, Tirunelveli, India, in 1988, and the M.E. degree from Anna University, Chennai, in 2009, and the Ph.D. degree from Karunya University, Coimbatore, India, in 2016. She was a Lecturer with Karunya University from 1988 to 1989. She was with the Government College of Engineering, Tirunelveli, from 1992 to 1998. She was a System Programmer with Computhink Computer Company, Al-Sharq, Kuwait, from 1998 2005. She has been a Tenured Professor with the Department of Information Technology, Francis Xavier Engineering College, Tirunelveli, since 2006. Her research interests include Medical Imaging, Biomedical Signal Processing and Digital image Processing. She has published several papers in International Journals and Conferences.

ELIJAH BLESSING RAJSINGH (M'06) received the M.Eng. degree (Hons.) and the Ph.D. degree in information and communication engineering from the College of Engineering, Anna University, Guindy, India, in 2005. He was the Director of the School of Computer Science and Technology, Karunya University from 2009 to 2015. He is currently the Director with Karunya University and a Professor in computer science and engineering. He joined Karunya University, Coimbatore, in 1997. His research areas include network security, mobile computing, wireless and ad hoc networks, medical image processing, parallel and distributed computing, grid computing, and pervasive computing. He has good number of publications. He has published articles in Elsevier, Springer, and Inderscience. He is an Associate Editor of the *International Journal of Computers and Applications*, Taylor and Francis. He is a member of the Editorial Review Board for many peer-reviewed journals. He has been identified as an Expert Member of the National Board of Accreditation, India. He is also being funded by Indian Council of Medical Research for his research project in Health systems research. He is a member of CSI and ISTE. He has served as an International Advisory Board Member for various International conferences and workshops.

GANESH R. NAIK (M'08–SM'15) received the B.E. degree in electronics and communication engineering from the University of Mysore, India, in 1997, the M.E. degree in communication and information engineering from Griffith University, Brisbane, Australia, in 2002, and the Ph.D. degree in electronics engineering from RMIT University, Melbourne, Australia, in 2009, with a focus on biomedical engineering and signal processing.

He has been the Chancellor's Post-Doctoral Research Fellow with the Faculty of Engineering and Information Technology, University of Technology Sydney, since 2013. He has edited ten books, and authored over 80 papers in peer-reviewed journals, conferences, and book chapters over the last seven years.

Dr. Naik serves as an Associate Editor of the IEEE Access and two Springer journals C*i*rcuits, S*y*stems, and S*i*gnal P*r*ocessing and A*u*stralasian P*h*ysical and E*n*gineering S*c*iences in M*e*dicine. He is a recipient of the Baden-Württemberg Scholarship from the University of Berufsakademie, Stuttgart, Germany from 2006 to 2007. In 2010, he received the ISSI Overseas Fellowship from the Skilled Institute Victoria, Australia.